Icarus 219 (2012) 57–76

Contents lists available at SciVerse ScienceDirect

Icarus

journal homepage: www.elsevier.com/locate/icarus

A comparison between rubble-pile and monolithic targets in impact simulations: Application to asteroid satellites and family size distributions

Paula G. Benavidez [a,b,c,*], Daniel D. Durda [c], Brian L. Enke [c], William F. Bottke [c], David Nesvorný [c], Derek C. Richardson [d], Erik Asphaug [e], William J. Merline [c]

[a] Departamento de Física, Ingeniería de Sistemas y Teoría de la Señal, Universidad de Alicante, P.O. Box 99, 03080 Alicante, Spain
[b] Instituto Universitario de Física Aplicada a las Ciencias y la Tecnología, P.O. Box 99, 03080 Alicante, Spain
[c] Southwest Research Institute, 1050 Walnut Street Suite 400, Boulder, CO 80302, USA
[d] University of Maryland, College Park, MD 20742, USA
[e] University of California Santa Cruz, CA 95064, USA

ARTICLE INFO

Article history:
Received 29 March 2011
Revised 18 January 2012
Accepted 19 January 2012
Available online 17 February 2012

Keywords:
Asteroids
Collisional physics
Impact processes
Satellites, General

ABSTRACT

Collisions are a fundamental process in the creation of asteroid families and in satellite formation. For this reason, understanding the outcome of impacts is fundamental to the accurate modeling of the formation and evolution of such systems. Smoothed-Particle Hydrodynamics/N-body codes have become the techniques of choice to study large-scale impact outcomes, including both the fragmentation of the parent body and the gravitational interactions between fragments. It is now possible to apply this technique to targets with either monolithic or rubble-pile internal structures. In this paper we apply these numerical techniques to rubble-pile targets, extending previous investigations by Durda et al. (Durda, D.D., Bottke, W.F., Enke, B.L., Merline, W.J., Asphaug, E., Richardson, D.C., Leinhardt, Z.M. [2004]. Icarus 170, 243–257; Durda, D.D., Bottke, W.F., Nesvorný, D., Enke, B.L., Merline, W.J., Asphaug, E., Richardson, D.C. [2007]. Icarus 186, 498–516). The goals are to study asteroid–satellite formation and the morphology of the size–frequency distributions (SFDs) from 175 impact simulations covering a range of collision speeds, impact angles, and impactor sizes. Our results show that low-energy impacts into rubble-pile and monolithic targets produce different features in the resulting SFDs and that these are potentially diagnostic of the initial conditions for the impact and the internal structure of the parent bodies of asteroid families. In contrast, super-catastrophic events (i.e., high-energy impacts with large specific impact energy) result in SFDs that are similar to each other. We also find that rubble-pile targets are less efficient in producing satellites than their monolithic counterparts. However, some features, such as the secondary-to-primary diameter ratio and the relative separation of components in binary systems, are similar for these two different internal structures of parent bodies.

© 2012 Elsevier Inc. All rights reserved.

1. Introduction

As a natural consequence of collisional evolution in the main asteroid belt, many asteroids have undergone a series of battering impacts that likely have left their interiors substantially fractured, if not completely rubblized. Chapman (1978) first used the term rubble-pile in the context of asteroid studies to describe a gravitationally bound collection of fragments resulting from sub-catastrophic impacts into asteroids (see Richardson et al., 2002). Such impacts may have enough energy to shatter and reassemble an object and not permanently disperse the fragments. The resulting structure will have moderate porosity because of the internal disorganization. Due to relatively weak gravitational self-cohesion between the constituent components, rubble-pile bodies may respond to subsequent impacts quite differently than would a more pristine, monolithic target. It is generally accepted to distinguish two main regimen, the so-called strength regime, where fragmentation is governed by the tensile strength of the target body and the gravity regime, where gravity is the dominant force. Recently a number of researchers have characterized the catastrophic threshold for different target materials (e.g. Jutzi et al., 2010; Leinhardt and Stewart, 2009).

Evidence supporting the existence of objects with a rubble-pile internal structure in the main-belt and near-Earth asteroid populations comes from observations, experiments and simulations (see Richardson et al. (2002) for a review). For instance, spacecraft observations of asteroids (e.g., Eros, Gaspra, Ida, Mathilde, Itokawa) and determination of the densities of primary objects in some observed binary systems suggest that many asteroids are fractured, shattered or perhaps have a rubble-pile internal structure (Sullivan

* Corresponding author at: Departamento de Física, Ingeniería de Sistemas y Teoría de la Señal, Universidad de Alicante, P.O. Box 99, 03080 Alicante, Spain.
E-mail address: paula.benavidez@ua.es (P.G. Benavidez).

0019-1035/$ - see front matter © 2012 Elsevier Inc. All rights reserved.
doi:10.1016/j.icarus.2012.01.015

et al., 2002; Fujiwara et al., 2006). In addition, most large main-belt asteroids with observed satellites are primitive (C-, F-, and P-types) (Merline et al., 2002) and are revealed to have low densities of order 1.3 g cm^{-3}. To be consistent with the expected carbonaceous chondrite meteorite analogs, these objects must have substantial porosity (Britt and Consolmagno, 2000). Other observational evidence includes crater chains and comet breakups such as the Comet D/Shoemaker–Levy 9 (SL9) at Jupiter.

Moreover, Farinella et al. (1982), using rotational data, studied the role of catastrophic collisions in the evolutions of asteroids. They claim that asteroids smaller than about 100 km are mostly multi-generation fragments, which arose in disruptive collisions, while for $D > 300$ km the collisional process produces nearly spheroidal objects covered by megaregolith. They suggest that almost all asteroids are outcomes of catastrophic collisions, and that these events cause either complete fragmentation of the target bodies or, at least, drastic readjustments of their internal structure, shape, and spin rate. After that, Cellino et al. (1985) studied the idea that the primary components of binary systems might be rubble-piles. This led them to propose a list of candidate binaries based on some features of the observed photometric behavior. On the other hand, Campo Bagatin and Petit (2001a) modeled numerically the collisional evolution of asteroids focusing on the response to impacts in terms of the different fraction of kinetic energy delivered to the fragments (f_{KE}). They estimated the abundance of re-accumulated objects (in the size range 10–200 km) to be between 50% and 100%, depending on the scaling law adopted and the f_{KE} parameter.

A typical impact between small bodies in the Solar System involves over 7 orders of magnitude more energy than impacts reproduced in laboratories. Therefore, laboratory experiments are limited to very small impactor sizes and moderate impact speeds. That limitation has motivated the development of new numerical techniques to simulate large-scale impacts. The techniques employ Smoothed-Particle Hydrodynamics (SPH) codes coupled with gravitational N-body codes capable of tracking the created fragments and their eventual re-accumulation. Michel et al. (2001) and Durda et al. (2004) showed that during the gravitational reaccumulation phase, multiple mutually orbiting systems could be created. Moreover, fragment interactions may allow the formation of large gravitational aggregates as a result of re-accumulation of smaller fragments. These results suggest that an important fraction of large family members could be the result of a gravitational reaccumulation of fragments produced after the parent body disruption (e.g. Michel et al., 2002).

Two interesting outcomes of collisions can be investigated with SPH/N-body models – creation of families and asteroid satellites. Understanding the formation mechanisms of such systems can lead to a better understanding of the collisional evolution of the main-belt. Concerning families, recent simulations of collisional destruction of asteroids reproduce quite well the main features of the size–frequency distributions (SFDs) of some asteroid families (Michel et al., 2001, 2002, 2003, 2004a,b; Nesvorný et al., 2006; Durda et al., 2007). However some families remain poorly represented, as pointed out by Durda et al. (e.g., the Eos and Astrid families). Recently, hybridized hydrocode/N-body method has also been used to investigate collision outcomes in a more general context of collisional evolution of small bodies in the Solar System and to understand the formation of the only detected Kuiper belt family Haumea (Leinhardt and Stewart, 2009; Leinhardt et al., 2010).

Regarding satellites, impacts are the most likely formation mechanism of satellites around the larger asteroids in the main-belt (Richardson and Walsh, 2006). For example, experiments of Durda et al. (2004), using undamaged rocky targets, have been successful at reproducing satellite system characteristics (e.g., satellite-to-primary mass ratios, semi-major axis distribution, etc.) of many observed main-belt asteroid binary systems (e.g. Merline et al., 2002). At present, 73 main-belt asteroid binaries are known (Johnston et al., 2010). Among the larger asteroids ($D > 140$ km) with satellites, we find that nearly all have no associated asteroid family. A related problem concerns two observed asteroid binaries that are essentially double asteroids. Both (90) Antiope and (617) Patroclus are ~100 km in diameter and have satellites that are comparable in size. Results from Durda et al. (2004) indicate that impacts onto undamaged rocky targets do not produce such relatively large binaries. These two outliers imply that the overall picture of binary formation is more complex, with occasional rare impact circumstances or multi-stage processes involved. Certainly, the observed TNO binaries could not be formed solely by the collisional processes modeled here, but must result from yet different or more complex processes. Nonetheless, we have shown that our current models reproduce well the characteristics of most of the satellites in the restricted class of larger ($\geqslant$10 km or so) main-belt asteroids. But the above discrepancies may be hinting that there is something important about asteroid satellite formation that could be missing in the current models; this formed part of the motivation for this paper.

Although SPH/N-body models are the best ones describing the effects of the propagation of shock waves into the impacted body in a rigorous way, there also are two different approaches that match very well some asteroid families. One of these approaches is a semiempirical model, based on the properties of a velocity field generated by the collision into a target body (Paolicchi et al., 1989, 1996). The second approach introduced by Tanga et al. (1999) is based on very simple geometric considerations. This latter numerical model assumes that fragments have convex shapes and take into account only geometric constrains imposed by the finite volume of the parent body and the fact that fragments should not overlap each other. Later, an improvement of the Tanga et al. model was presented by Campo Bagatin and Petit (2001b). The main feature of this new model is that they simulated the largest remnant in a more realistic way, considering the possibility of changing the shape of the largest remnant as the mass ratio between the largest fragment and target body changes. Both numerical approaches reproduce quite well the features of asteroid families for sizes bigger than 10 km, but produce steeper slopes of the SFD in many cases for smaller sizes. Also these kinds of models cannot give us information about the impact conditions like the impact speed and impactor size, which could be useful to understand the collisional evolution of the asteroid belt.

A critical factor that has not yet been deeply and systematically explored, but one that could potentially be relevant to the above issues, concerns the internal structure of the parent body. To address this, we focus on the following goals. The first is to investigate asteroid satellite formation via impacts onto rubble-pile targets and to compare the results with those of Durda et al. (2004). The second is to study the rubble-pile SFD morphologies and to compare them with the SFDs resulting from monolithic simulations of Durda et al. (2007). Finally, as a by-product of this comparative study, we aim to determine which families are best represented by models of rubble-pile versus monolithic targets.

This paper is organized as follows. In Section 2, we present a description of the numerical model. In Section 3, the results of the comparison between our systematic numerical investigation on rubble-pile versus monolithic targets are presented. In Section 4, a comparison between results from our numerical models and observed main-belt binary systems and asteroid families is discussed. Finally, in Section 5, we present our conclusions.

2. Numerical technique

The results presented here were obtained by applying, for the most part, the same numerical techniques as those used in Durda

et al. (2004, 2007). We summarize here the main features of the technique.

Durda et al. (2004) substantially improved upon earlier models dedicated to studying asteroid satellite formation (e.g. Hartmann, 1979; Durda, 1996; Doressoundiram et al., 1997) by taking advantage of state-of-the-art numerical tools. The new techniques included: (1) a Smoothed-Particle Hydrodynamic (SPH) code, which models the pressures, temperatures, and energies of asteroid–asteroid impacts, and (2) an efficient N-body code, which can track the trajectories of hundreds of thousands of individual collision fragments in an expedient manner. Initially, the SPH code is used to model the actual impact. Then, when the impact simulations are sufficiently complete (crater formation/ejecta flow fields established with no further fragmentation/damage), the outcomes of the SPH models are handed off as the initial conditions for N-body simulations, which follow the trajectories of the ejecta fragments for an extended time to search for the formation of bound satellite systems. This is essentially the same numerical scheme utilized by Michel et al. (2001, 2002) to study the formation of asteroid families. Below, we briefly summarize the SPH and N-body simulation techniques.

2.1. Smoothed-Particle Hydrodynamic simulations

We modeled the collision phase of cratering and catastrophic impacts between two asteroids with the 3-D SPH code SPH3D (Benz and Asphaug, 1995). That code models shock propagation in elastic solids, utilizing a plastic yield criterion for intense deformation, together with an explicit fracture and dynamic fragmentation model acting on the principal tensile component of the stress tensor during brittle deformation. The results presented here are not sensitive to the parameters used in our fragmentation model, because damage – the measure of the elastic strength – is total, throughout both impacting bodies, by the end of these calculations. The fracture model does, however, affect the coupling of impact energy into the target, including the behavior of the back spall zone. We adopt fracture parameters appropriate for terrestrial basalt (see Asphaug et al., 2002, for a table of these parameters).

The equation-of-state model used is that of Tillotson (1962); it is based on the linear relationship between shock speed and particle velocity (see Appendix II of Melosh, 1989, for a detailed description). While more sophisticated equations of state can be adopted, that of Tillotson is well understood, and gives excellent results when compared with ejecta velocities derived from laboratory impact experiments (Benz and Asphaug, 1994, 1995).

Gravitational self-compression of the target during the impact phase is treated as an overburden stress that must be exceeded before fracture can initiate (Asphaug and Melosh, 1993). In Durda et al. (2004), we found that the modeled collision outcomes for targets with 100,000 or more particles matched each other sufficiently well, leading us to conclude that we achieved resolution convergence for fragments of a few to several kilometers in diameter.

For the present study, we simulated impacts between a monolithic impactor and a rubble-pile target, using almost the same matrix of impact parameters as Durda et al. (2004). We construct rubble-pile targets (see Asphaug et al., 2002) by filling the interior of the 100-km-diameter spherical shell (the target envelope) with an uneven distribution of solid basalt spheres having diameters between 8 km and 20 km. We then decrease the density and strength of SPH particles in the contact zones between the solid components from 2.7 to 1.3 g cm^{-3} as a way to represent the damage (Fig. 1 shows an example of our target body). The remainder of the target body is void space. Resolution is of concern, and to ensure physical modeling we require at least ~5 particles across the smallest rubble-pile spheres of the target, to capture the shock.

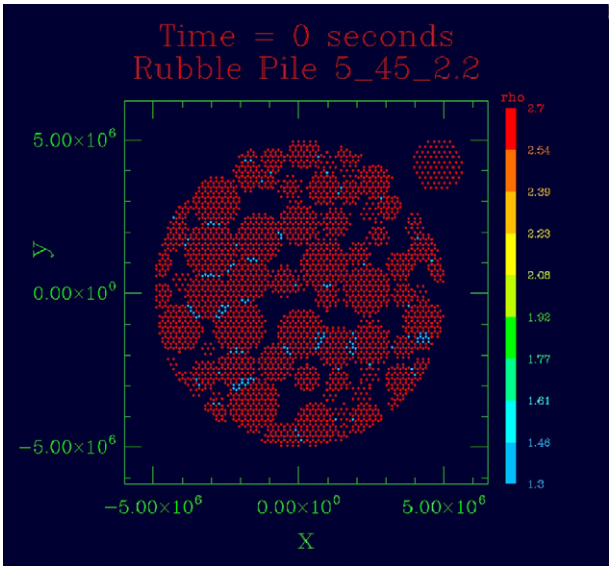

Fig. 1. Image of our rubble-pile target taken before impact. Contact zones between the target components have different densities as the color bar on the right indicates. (For interpretation of the references to color in this figure legend, the reader is referred to the web version of this article.)

This results in the lower boundary for the diameter of the basalt spheres stated above (8 km).

2.2. N-body simulations

Once the SPH impact phase of the simulation is finished (i.e., fracture is complete and ejecta velocity flow is well established), the outcomes of the SPH models are handed off as the initial conditions for N-body simulations. The N-body code tracks the dynamical evolution and any subsequent fragment–fragment collisions. To track the trajectories of collision fragments we use the cosmological N-body code pkdgrav (Stadel, 2001), modified as described in Richardson et al. (2000) (see also Leinhardt et al., 2000; Leinhardt and Richardson, 2002). Pkdgrav is a scalable, parallel tree code for modeling the gravitational interactions between particles. A unique feature of this code is the ability to rapidly detect and accurately treat low-speed collisions between particles (with or without self-gravity), even at the extreme limits seen in dense granular media such as sand-piles (Richardson et al., 2011; Tanga et al., 2009). This allows for realistic modeling of the formation of rubble-pile accumulations among ejected fragments.

The tree component of the code provides a convenient means of consolidating forces exerted by distant particles, reducing the computational cost. The parallel component divides the work evenly among available processors, adjusting the load at each time-step according to the amount of work done in the previous force calculation. The code uses a straightforward second-order leapfrog scheme for the integration and computes gravity moments from tree cells to hexadecapole order. Particles are considered to be finite-sized hard spheres and collisions are identified during each time step using a fast neighbor-search algorithm. Low-speed collisions between debris fragments are treated as mergers resulting in a new spherical particle of appropriate combined mass and equivalent diameter. We set the merged density to the starting bulk density of the target, which is 1.835 g cm^{-3} for most of these simulations.

The N-body simulations are run, with time steps equal to 10^{-5} in units of year/2π (e.g., ~50 s), to a time about 17.5 days (i.e., 30,000 time steps) after the impact. Our choice of 17.5 days of N-body simulation time after impact was set by a combination of

available CPU resources and because the number of satellites and satellite systems that one would expect to see due to formation and dissolution of transient binaries should not change significantly after that time. Limitations inherent in the simulations due to the fact that irregular primary asteroid shapes are not preserved and therefore mutual tidal interactions are not included.

We use a hierarchical 3-D spatial tree code (`companion`; Leinhardt and Richardson, 2005) to search for bound pairs in the output. As with gravity tree codes, this method reduces the search cost to order $N \log N$ by considering only nearby particles, or members of more distant particle groups with low relative bulk motion, as potential companions. The search is parameterized by the standard tree cell opening-angle criterion, a quality factor that trades off computing cost versus finding all possible binaries (e.g. Barnes and Hut, 1986); the default of 0.25 radian used in `companion` is quite conservative and is based on the assumption that searches will be conducted infrequently on a given data set. In principle, very distant companions could be missed, but thorough testing shows that over 99% of binaries are found in most cases. It is possible that catastrophic collisions could produce more complex multiple systems. `Companion` can do searches both for systems where the satellite is bound to only one primary and for hierarchical systems. To be consistent with previous analyses published by Durda et al. (2004), we only search for satellites bound to one primary. However, as was pointed out by Leinhardt and Richardson (2005), and also confirmed in this work, the difference in the number of binary systems found using both options is, in general, less than 0.5%.

2.3. Hand off between SPH and N-body simulations

Converting the `SPH3D` output into input parameters for `pkdgrav` is a multi-step process where we adopt several approximations.First, we had to account for the different representations of particles in the two codes. SPH particles are not really particles, but instead represent overlapping Gaussian distributions with fixed densities. When these particles are converted into the hard-sphere particles utilized in `pkdgrav`, they cannot maintain the same density or size because `pkdgrav` does not normally deal with overlapping particles. To overcome this problem, we modified the size and density of each `pkdgrav` particle, ensuring that mass is conserved. Thus, the initial size of each `pkdgrav` particle is smaller than that in the SPH code, while their densities are slightly higher.

Second, for this later phase of evolution we assume that all particle collisions result in accretion. This is reasonable for the relative speeds of interest (tens of m s^{-1}). When particles collide, we force them to merge into a single body. This approximation compels most of the particles in the target body to merge into a single particle before the end of the simulation. We do this to avoid having to compute numerous collisions between adjacent bodies that have essentially zero relative speeds. A different approach could be considered for modeling the physical processes that occur during reaccumulation onto the largest remnant. Leinhardt and Stewart (2009) already studied this issue for the cases of perfect merging (for which the coefficient of restitution, ϵ_n, is effectively zero), conditional merging (which depends on the speed of the particles with respect to the escape speed), and inelastic bouncing ($\epsilon_n > 0$, no merging). They found that even though some differences are seen for the largest remnant in the two extreme cases (merging versus bouncing), simple merging is generally adequate given that the majority of the collisions occur between particles that are gravitationally bound to the largest remnant.For the present work we have conducted several tests of runaway accretion by studying initial particle velocities/locations and also turning on particle "bouncing" during the first 100 N-body time steps for two test simulations. In one of our test runs we see almost no difference in the largest remnant, but in another, more energetic impact, we see a ~15% shrinkage in the largest remnant diameter. We also noticed potential differences in the number of SMATS/EEBs and the SFDs in both simulations. In particular, the quoted estimates of the number of SMATS/EEBs for most runs may end up being quite conservative (more SMTAS/EEBs than estimated in this work). We hesitate to draw any sweeping conclusions from only these test runs, especially since "bouncing" parameters must be carefully tuned to keep the physics as realistic as possible (i.e., in attempting to fix overzealous merging we might create overzealous bouncing). In summary, the number of SMATS/EEBS, size of the largest remnant, and SFD in some simulations may be sensitive to when we begin the N-body merging steps. Newer (rigid N-body, and possibly soft-sphere N-body) techniques will be used to explore the extent of the issue in future work.

2.4. Analyzing different configurations of the target and orientation

Unlike previous solid monolithic targets (Durda et al., 2004), our rubble-pile targets have an inhomogeneous internal mass distribution. The exact orientation of the target with respect to the incoming projectile can therefore affect the impact outcome. We performed additional simulations to study the effects of different internal rubble-pile configurations while preserving the overall size–frequency distribution of the solid spheres. We have also rotated the target by ±1° about two axes, for studying the effects of minor changes in the target body orientation.

Before describing the simulation results we introduce the nomenclature we use to refer to the output of a particular impact simulation, with respect to the target structure/composition, the impact speed, the impact angle, and the logarithm of the target-to-impactor mass ratio. We follow here the same nomenclature used in Durda et al. (2004, 2007). For example, simulation "rubble-pile_4_45_1.8" involved a 100-km-diameter rubble-pile target, impacted at 4 km s^{-1} at a 45° impact angle and logarithm of the target-to-impactor mass ratio equal to 1.8, it said by a 25-km-diameter projectile. We refer to the corresponding solid-target run from our previous matrix of impact simulations as "monolithic_4_45_1.8". We also define the equivalent SMATS[1] ("SMAshed Target Satellite") diameter as the average diameter of all SMATS around a given largest remnant. Fig. 2 shows the result for both studied issues (different internal configurations and orientations). In particular Fig. 2a shows the equivalent SMATS diameter as a function of the largest remnant diameter (D_{lr}) for two different cases: 4_45_1.8 and 5_45_3.0. For both cases we observe some variation of the results between different simulations due to different target configurations. When we rotated the target with a given configuration the results turned out to be more similar to each other. The SFDs seem quite similar for different target configurations, within the variations for the largest remnant detailed above (see Fig. 2b and c).

We observe that the simulation results are more sensitive to the specific orientation of the target body when smaller impactors are considered. However, despite orientation-dependent variations from run to run, the results of each simulation follow the general trend (see Section 3). In order to avoid a systematic, built-in bias to the results that might occur with any one specified target orientation, the target configuration was randomized for each run, thus statistically smoothing out the variations in impact outcome from run to run.

3. Results

We now turn to the presentation of our rubble-pile results, obtained by applying the methods introduced in Section 2 to our full

[1] More details about SMATS are given in Section 3.

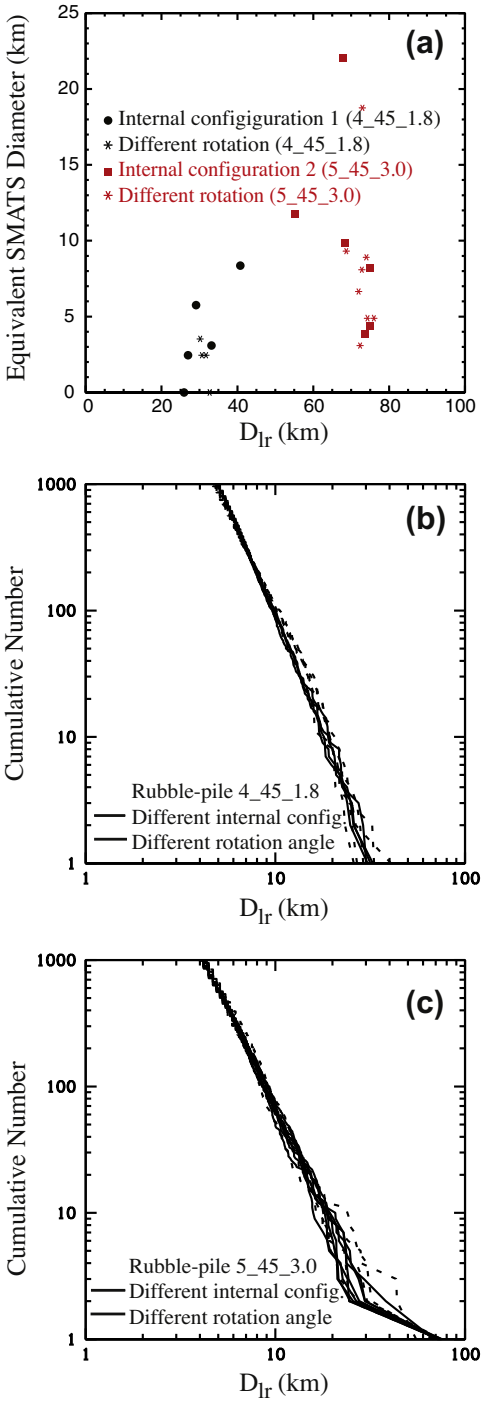

Fig. 2. Comparison between different target internal distribution and impact angles changed in ±1°. Simulations present some variation in the size of the largest remnant.

sample of 175 simulations. The non-rotating targets, 100 km in diameter, are assumed to be spherical and are composed of a rubble-pile internal structure with a bulk density of 1.84 g cm^{-3}. The monolithic spherical impactor diameters are 7, 10, 14, 18, 25, 34, and 46 km, which correspond to 3.4, 3.0, 2.6, 2.2, 1.8, 1.4 and 1.0 in logarithm of the target-to-impactor mass ratio, respectively. Impact speeds range from 3 to 7 km s^{-1}, and impact angles range from 15° to 75° (nearly head-on to very oblique) in 15° increments. Note that with respect to the monolithic simulations of Durda et al. (2004) we performed an extra set of simulations with a logarithm of the target-to-impactor mass ratio equal to 3.4 (smaller impactor, ~7 km). Impact initial conditions and outcomes are listed for each simulation in Table 1. Here we examine the statistical properties of the resulting binary systems and the morphology of SFDs as a function of impact initial conditions. As in Durda et al. (2004), we found that some impact debris can enter into orbit around the remaining target body, which is a gravitationally re-accreted rubble-pile, to form SMATS ("SMAshed Target Satellite"). On the other hand, there are numerous smaller fragments escaping the largest remnant and some may have similar trajectories such that they are bound to one another, forming EEBs ("Escaping Ejecta Binaries").

3.1. Largest remnant versus specific impact energy

Fig. 3 shows the largest remnant diameter as a function of the specific impact energy ($Q = E_c/M_T$, where E_c is the impact kinetic energy and M_T is the target mass) for rubble-pile and monolithic targets. Here we define a catastrophic impact as an impact that breaks a body into a spectrum of intact fragments, with the largest one having half or less of the mass of the original target. We call super-catastrophic and sub-catastrophic events those impacts with substantially higher and less energy, respectively, than those that produce a catastrophic impact. As expected, the largest remnant diameter shows a strong dependence on impact conditions. Smaller impactors produce cratering impacts, leaving a bigger largest remnant, as do collisions with more oblique impact angles and lower impacts speeds. There is an important general trend that the largest remnants from rubble-pile targets are generally smaller than monolithic ones. For rubble-pile targets suffering impacts at a very oblique angle or from smaller impactors at any impact angle, the typical result is a sub-catastrophic impact, while for monolithic targets, under the same impact conditions, only a cratering event results. That response could be because our rubble-pile targets are less dense than the monolithic ones, leading to a less efficient gravitational re-accumulation on the largest remnant. Also, the manner in which we have constructed our approximation of a rubble-pile target (essentially a cluster of smaller solid targets loosely "glued" together) results in a loose collection of boulders. In such situations, considerable impact energy may simply go toward pushing objects out of the way rather than breaking them down into smaller bits. Real rubble-piles probably also have component porosity (Jutzi et al., 2010) and a more complete power-law tail of much smaller debris, which we have not included and that might absorb more of the impact energy.

3.2. SMATS

Fig. 4a shows the resulting equivalent SMATS diameters (see definition in Section 2.4) as a function of the diameter of the largest remnant for a rubble-pile parent body. In this figures, super-catastrophic and sub-catastrophic impacts are represented to the far left and right respectively (leaving a catastrophic impact with largest remnant diameter around 80 km). As in the case of monolithic targets (see Fig. 5a, reproduced from simulation results of Durda et al., 2004), the largest SMATS are formed around the largest remnant of moderately catastrophic impacts. For rubble-pile targets, however, the equivalent SMATS diameters have a more spread distribution than for monolithic targets. Comparing Figs. 4 and 5a, we see that for rubble-pile targets even high speeds are efficient in producing relatively large satellites around the largest remnant, in contrast to the slow speeds required for monolithic targets.

Fig. 4b shows the number of SMATS versus the diameter of the largest remnant for rubble-pile targets and Fig. 5b shows the same, but for monolithic ones. SMATs are produced less efficiently for rubble-piles, especially for big impactors at 15°, 30° and 45° impact angles. However, that behavior changes when the smallest

Table 1
Results of 175 SPH/N-body simulations.

Impact speed (km s^{-1})	Impact angle (°)	log (M_{trag}/M_{imp})[a]	Largest remnant diameter (km)	M_{lr}/M_{targ}[b]	Number of SMATS	SMATS equivalent diameter[c] (km)	Number of EEB primaries	Number of EEB secondaries	Largest EEB primary (km)	Largest EEB secondary (km)
3	15	1.0	43.95	0.0849	8	8.24	39	39	23.31	4.90
3	15	1.4	29.85	0.0266	0	–	44	44	8.52	3.89
3	15	1.8	26.80	0.0193	0	–	39	39	11.89	6.05
3	15	2.2	25.37	0.0163	1	3.89	82	87	22.87	8.10
3	15	2.6	43.52	0.0824	16	12.50	115	157	35.95	8.84
3	15	3.0	82.84	0.5686	12	7.78	69	87	23.99	12.12
3	15	3.4	90.40	0.7388	1	2.45	122	160	21.42	8.71
3	30	1.0	19.71	0.0077	0	–	42	43	18.57	4.69
3	30	1.4	19.65	0.0076	0	–	40	40	12.30	7.45
3	30	1.8	26.36	0.0183	0	–	69	72	23.74	6.04
3	30	2.2	45.22	0.0925	3	7.44	94	114	33.73	9.95
3	30	2.6	69.80	0.3400	11	11.14	119	163	27.49	7.86
3	30	3.0	75.49	0.4302	28	12.41	106	160	27.98	10.24
3	30	3.4	90.82	0.7492	3	5.76	85	134	33.51	13.47
3	45	1.0	22.11	0.0108	0	–	44	44	18.70	6.30
3	45	1.4	28.56	0.0233	0	–	37	38	19.86	15.31
3	45	1.8	40.06	0.0643	1	2.45	71	83	39.68	24.76
3	45	2.2	46.50	0.1005	11	12.08	113	153	42.05	34.29
3	45	2.6	75.21	0.4254	7	9.85	91	125	27.77	9.85
3	45	3.0	82.65	0.5645	4	4.19	82	131	26.94	12.79
3	45	3.4	90.86	0.7500	0	–	103	132	19.43	9.48
3	60	1.0	48.84	0.1165	1	3.89	61	63	26.13	13.05
3	60	1.4	60.47	0.2211	1	11.02	80	92	30.66	19.76
3	60	1.8	61.97	0.2379	12	9.20	92	119	22.87	11.78
3	60	2.2	76.96	0.4559	3	4.69	93	126	27.57	12.66
3	60	2.6	85.27	0.6199	4	4.19	91	128	25.85	13.20
3	60	3.0	89.99	0.7287	6	4.45	52	67	20.01	8.09
3	60	3.4	93.30	0.8121	0	–	61	74	21.01	5.45
3	75	1.0	82.53	0.5621	1	2.45	78	120	51.59	9.95
3	75	1.4	84.48	0.6029	3	4.69	90	135	31.32	11.81
3	75	1.8	88.25	0.6873	4	3.89	53	63	18.18	7.86
3	75	2.2	89.85	0.7253	1	2.45	64	78	25.73	8.02
3	75	2.6	92.75	0.7979	5	6.04	39	52	21.36	6.86
3	75	3.0	94.19	0.8356	1	5.76	55	68	17.31	6.54
3	75	3.4	95.17	0.8621	1	2.45	45	49	12.09	5.10
4	15	1.0	15.76	0.0039	0	–	27	27	12.38	4.19
4	15	1.4	19.97	0.0080	0	–	30	30	12.38	4.69
4	15	1.8	17.94	0.0058	0	–	59	60	8.60	5.62
4	15	2.2	20.95	0.0092	1	4.69	70	73	17.11	5.90
4	15	2.6	40.15	0.0647	1	2.45	133	175	29.45	11.88
4	15	3.0	48.99	0.1176	28	16.90	128	196	46.44	13.05
4	15	3.4	80.14	0.5147	7	6.76	134	248	31.72	10.77
4	30	1.0	19.54	0.0075	0	–	36	36	12.37	3.53
4	30	1.4	15.90	0.0040	0	–	50	50	13.02	3.89
4	30	1.8	19.97	0.0080	0	–	59	63	16.45	5.61
4	30	2.2	29.39	0.0254	5	12.69	95	100	29.04	8.52
4	30	2.6	48.48	0.1139	9	6.42	130	197	35.35	19.79
4	30	3.0	51.52	0.1368	16	13.02	93	211	49.23	34.36
4	30	3.4	88.11	0.6840	0	–	112	158	18.86	8.52
4	45	1.0	22.36	0.0112	0	–	55	55	13.03	4.70
4	45	1.4	24.16	0.0141	0	–	48	49	19.43	13.92
4	45	1.8	33.40	0.0372	2	7.07	94	99	23.70	10.60
4	45	2.2	33.61	0.0380	1	2.45	106	132	31.45	14.31
4	45	2.6	49.31	0.1199	20	16.28	129	215	44.83	16.57
4	45	3.0	79.94	0.5108	6	5.61	90	118	23.94	20.68
4	45	3.4	88.92	0.7031	17	7.44	90	114	20.22	11.25
4	60	1.0	31.61	0.0316	2	3.09	43	48	30.77	7.44

4	60	1.4	37.05	0.0508	0	–	90	98	36.34	10.57
4	60	1.8	63.85	0.2603	5	5.45	81	100	39.03	13.73
4	60	2.2	67.95	0.3137	13	8.58	92	128	37.79	10.73
4	60	2.6	81.15	0.5345	11	5.90	99	144	29.87	7.69
4	60	3.0	87.83	0.6775	8	6.30	84	99	21.81	14.43
4	60	3.4	91.13	0.7568	1	2.45	114	142	21.26	7.86
4	75	1.0	77.10	0.4584	9	6.65	105	154	46.35	11.33
4	75	1.4	80.03	0.5126	3	4.19	111	172	31.71	10.06
4	75	1.8	87.96	0.6805	6	6.04	85	115	20.69	7.16
4	75	2.2	88.47	0.6925	1	2.45	55	75	27.11	13.62
4	75	2.6	92.27	0.7856	3	5.45	61	73	16.37	6.97
4	75	3.0	92.46	0.7903	0	–	61	74	14.68	7.35
4	75	3.4	94.43	0.8419	17	10.43	58	69	21.37	5.45
5	15	1.0	14.40	0.0030	0	–	9	9	3.09	2.45
5	15	1.4	11.26	0.0014	0	–	31	31	11.03	3.89
5	15	1.8	15.21	0.0035	0	–	75	77	13.52	5.28
5	15	2.2	17.39	0.0053	0	–	67	68	15.10	7.94
5	15	2.6	29.75	0.0263	3	4.45	109	122	21.45	13.58
5	15	3.0	59.60	0.2117	25	17.77	133	175	33.01	10.05
5	15	3.4	82.05	0.5523	15	7.17	150	207	30.00	14.19
5	30	1.0	11.22	0.0014	0	–	38	38	6.04	3.09
5	30	1.4	14.88	0.0033	0	–	64	65	9.09	3.89
5	30	1.8	16.62	0.0046	0	–	60	63	15.19	8.38
5	30	2.2	26.23	0.0180	1	2.45	68	75	20.88	12.88
5	30	2.6	29.27	0.0251	2	3.09	135	147	24.01	9.20
5	30	3.0	51.28	0.1348	31	12.15	105	240	48.40	19.42
5	30	3.4	86.75	0.6528	1	3.54	127	165	18.64	8.38
5	45	1.0	17.08	0.0050	0	–	57	58	10.60	6.97
5	45	1.4	24.27	0.0143	0	–	61	65	15.89	5.61
5	45	1.8	23.76	0.0134	0	–	59	62	17.23	7.61
5	45	2.2	30.46	0.0283	1	2.45	91	100	28.69	14.47
5	45	2.6	46.10	0.0979	20	12.90	117	170	30.05	13.55
5	45	3.0	74.95	0.4210	27	15.78	111	159	25.90	13.10
5	45	3.4	89.20	0.7098	2	3.54	79	96	21.22	8.31
5	60	1.0	33.50	0.0376	1	3.09	58	58	20.10	7.17
5	60	1.4	38.16	0.0556	1	7.53	118	127	26.34	12.42
5	60	1.8	46.23	0.0988	5	4.45	90	109	39.04	9.08
5	60	2.2	65.09	0.2758	7	6.76	98	139	32.40	17.54
5	60	2.6	69.79	0.3399	22	13.96	121	181	28.54	17.14
5	60	3.0	86.49	0.6469	2	3.09	81	122	25.05	10.90
5	60	3.4	91.09	0.7558	4	7.16	82	116	22.02	8.96
5	75	1.0	77.98	0.4741	2	7.26	116	164	45.98	10.24
5	75	1.4	80.90	0.5295	5	5.10	91	162	27.19	9.90
5	75	1.8	83.09	0.5736	15	6.76	95	159	25.37	11.99
5	75	2.2	86.09	0.6381	1	3.09	83	132	22.67	10.98
5	75	2.6	91.98	0.7781	7	6.97	35	38	22.28	8.52
5	75	3.0	93.53	0.8182	0	–	53	63	20.93	5.77
5	75	3.4	93.12	0.8074	0	–	53	61	17.94	8.85
6	15	1.0	8.84	0.0007	0	–	7	7	3.08	2.45
6	15	1.4	9.75	0.0009	0	–	30	30	7.35	3.09
6	15	1.8	11.67	0.0016	0	–	46	47	9.90	5.28
6	15	2.2	13.80	0.0026	0	–	51	51	13.07	3.89
6	15	2.6	21.64	0.0101	0	–	83	89	16.63	7.86
6	15	3.0	38.06	0.0551	1	2.45	127	186	38.03	9.70
6	15	3.4	56.20	0.1775	49	20.68	214	343	42.35	10.60
6	30	1.0	8.38	0.0006	0	–	25	25	4.90	2.45
6	30	1.4	13.17	0.0023	0	–	34	34	8.25	3.09
6	30	1.8	14.09	0.0028	0	–	60	60	8.59	5.45
6	30	2.2	21.66	0.0102	0	–	80	84	17.17	5.10
6	30	2.6	24.25	0.0143	2	3.53	107	115	20.83	7.44
6	30	3.0	58.17	0.1969	15	9.20	150	196	35.45	11.14
6	30	3.4	74.65	0.4160	51	23.66	87	131	30.52	13.55

(*continued on next page*)

Table 1 (*continued*)

Impact speed (km s^{-1})	Impact angle (°)	log (M_{trag}/M_{imp})[a]	Largest remnant diameter (km)	M_{lr}/M_{targ}[b]	Number of SMATS	SMATS equivalent diameter[c] (km)	Number of EEB primaries	Number of EEB secondaries	Largest EEB primary (km)	Largest EEB secondary (km)
6	45	1.0	14.38	0.0030	0	–	49	49	11.78	3.09
6	45	1.4	16.90	0.0048	0	–	51	52	11.45	3.54
6	45	1.8	22.81	0.0119	1	3.09	66	70	15.20	7.53
6	45	2.2	30.36	0.0280	4	8.79	89	97	25.33	12.09
6	45	2.6	23.20	0.0125	1	3.53	142	157	21.13	10.29
6	45	3.0	58.42	0.1994	23	19.19	122	184	43.19	10.24
6	45	3.4	81.60	0.5434	35	10.99	83	133	22.47	13.45
6	60	1.0	34.94	0.0427	3	13.88	72	78	32.15	6.86
6	60	1.4	24.87	0.0154	1	3.09	84	91	22.56	9.08
6	60	1.8	32.00	0.0328	2	4.69	90	95	27.59	8.52
6	60	2.2	54.59	0.1627	7	9.20	131	185	31.40	11.77
6	60	2.6	51.66	0.1379	14	7.87	120	213	46.82	9.72
6	60	3.0	81.18	0.5349	5	10.94	109	165	29.33	13.05
6	60	3.4	88.62	0.6959	6	5.28	61	90	22.71	10.19
6	75	1.0	66.42	0.2930	6	9.75	165	210	41.08	11.41
6	75	1.4	65.30	0.2785	7	5.28	130	184	36.17	12.15
6	75	1.8	80.23	0.5164	10	9.65	115	183	39.13	11.22
6	75	2.2	82.88	0.5694	14	9.26	80	112	32.17	11.67
6	75	2.6	90.40	0.7387	1	2.45	62	84	18.40	8.84
6	75	3.0	90.79	0.7484	1	3.09	64	73	21.63	8.90
6	75	3.4	91.47	0.7654	2	3.09	83	107	16.64	7.94
7	15	1.0	6.42	0.0003	0	–	5	5	2.45	2.45
7	15	1.4	5.76	0.0002	0	–	18	18	3.09	2.45
7	15	1.8	8.31	0.0006	0	–	38	38	5.45	3.53
7	15	2.2	13.93	0.0027	0	–	54	54	10.56	5.45
7	15	2.6	18.96	0.0068	0	–	101	105	14.14	6.65
7	15	3.0	24.86	0.0154	3	4.90	152	170	23.61	11.06
7	15	3.4	82.73	0.5661	1	2.45	30	39	32.45	11.45
7	30	1.0	6.04	0.0002	0	–	20	20	5.10	2.45
7	30	1.4	11.81	0.0016	0	–	25	25	3.53	2.45
7	30	1.8	13.05	0.0022	0	–	69	70	11.11	5.61
7	30	2.2	16.16	0.0042	1	2.45	74	75	15.04	4.90
7	30	2.6	26.67	0.0190	1	2.45	103	109	19.88	6.97
7	30	3.0	26.77	0.0192	8	5.76	131	163	25.31	9.80
7	30	3.4	62.92	0.2491	36	16.31	120	195	43.06	10.47
7	45	1.0	13.38	0.0024	1	2.45	65	65	6.76	4.69
7	45	1.4	14.16	0.0028	0	–	76	76	10.05	5.28
7	45	1.8	19.29	0.0072	0	–	81	82	15.47	5.45
7	45	2.2	17.03	0.0049	1	2.45	76	81	14.70	5.61
7	45	2.6	36.91	0.0503	4	4.69	113	136	21.21	10.33
7	45	3.0	52.18	0.1421	16	16.87	122	169	35.96	13.89
7	45	3.4	72.76	0.3852	62	24.57	128	185	26.64	12.54
7	60	1.0	46.71	0.1019	0	–	70	72	15.92	6.97
7	60	1.4	30.55	0.0285	0	–	64	70	29.52	10.40
7	60	1.8	56.14	0.1770	3	4.45	25	25	15.78	8.65
7	60	2.2	41.01	0.0690	18	17.31	138	172	28.39	21.27
7	60	2.6	51.06	0.1331	8	16.05	135	208	47.07	17.15
7	60	3.0	84.30	0.5992	9	9.49	91	121	27.51	11.74
7	60	3.4	86.74	0.6527	3	3.89	84	120	30.31	18.97
7	75	1.0	70.18	0.3456	38	15.90	163	210	27.07	10.10
7	75	1.4	73.28	0.3934	4	8.09	128	161	30.79	14.31
7	75	1.8	77.57	0.4667	5	5.61	109	167	22.07	15.54
7	75	2.2	82.63	0.5642	3	3.53	95	152	25.75	11.10
7	75	2.6	86.66	0.6508	7	5.61	93	126	24.32	9.80
7	75	3.0	91.16	0.7575	9	8.09	76	96	17.11	9.54
7	75	3.4	92.25	0.7852	0	–	92	111	21.94	7.26

[a] Logarithm of target to impactor mass ratio.
[b] Largest remnant to target mass ratio.
[c] Average diameter of all SMATS around a given largest remnant.

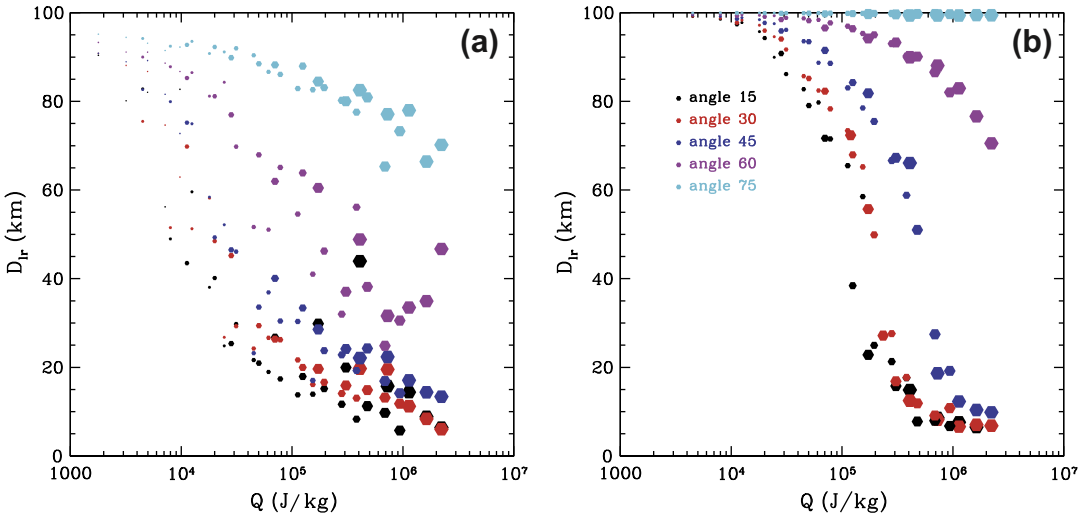

Fig. 3. Largest remnant diameter versus specific impact energy for (a) rubble-pile target and (b) monolithic target. Dot sizes are coded according to impactor diameter, smaller dots represent smaller impactors (which size are: 7, 10, 14, 18, 25, 34 and 46 km). Note that some deviation of the evident general trend are expected in the largest fragment diameter due to the random internal distribution (see Section 2.4).

impactor is considered for the same angles and medium-sized and largest impactors for 60° and 75°, respectively. In other words, the maximum number of SMATS are produced by $\log(M_{targ}/M_{imp})$ ~2.6 to ~3 (impactors of ~10 to ~14 km) at almost head-on impacts; these collisions left a largest remnant around 50–60% of the target diameter. In the case of 75° impact angle, larger impactors are needed to get almost similar number of SMATS.

Figs. 4 and 5a show an arc trend, leaving a paucity in the largest remnant diameter from ~50 to ~80 km for rubble-piles, and from ~20 to ~60 km for monolithic targets. That paucity is the consequence of the strong dependence between the size of the largest remnant and the impact energy. On the other hand, a high-energy impact (big impactors) on a rubble-pile target left very few and smaller SMATs than in case of monolithic targets.

3.3. EEBs

Figs. 6 and 7 show the largest EEB primary diameter and the number of EEBs created in each simulation, as a function of the diameter of the largest remnant for rubble-pile and monolithic targets, respectively. The largest EEB primary diameter increases linearly with the largest remnant diameter for impact angles as oblique as 45° and becomes more spread for more oblique impacts. The number of EEBs increases also with the largest remnant size, but the trend is somewhat more bow-shaped. The highest target-to-impactor mass ratios (or the smallest impactors) produce more and larger EEBs when the impact angle is as oblique as 60°, while when the impact angle is 75° the largest impactors are what produce more and bigger EEBs.

In the monolithic case, moderately catastrophic impacts at low speed produced a large amount of EEBs, but for rubble-pile targets the largest number of EEBs is not limited to low impact speeds. However, the maximum number of EEBs from rubble-pile targets is about a factor ~7 lower than from monolithic parent bodies (see Fig. 7). It is interesting to note that when monolithic targets are impacted at 75° very large EEBs are produced. In these cases not much energy is transferred in the impact and the target is hardly damaged. These large EEB primaries are thus formed from the projectile material, much of which remains intact as the projectile "shears off" a side of the target. The fact that few binaries are observed in asteroid families may suggest that the parent bodies of these families may be rubble-piles (cf. Section 4).

3.4. SFD morphologies

Fig. 8 shows a wide range of morphologies of the fragment SFDs resulting from our rubble-pile simulations, compared with the monolithic runs from Durda et al. (2004), Durda et al. (2007). For rubble-pile targets, as was true for monolithic targets, low-energy impacts (produced by small impactors and/or oblique impacts) result in cratering events, while high-energy impacts (mainly large impactors) result in catastrophic or super-catastrophic events. No significant changes are observed in the general morphology of the SFDs by varying the impact speed for a given size impactor and angle (except for a minor features discussed below). In particular, for an impact angle of 75°, the shape of rubble-pile SFDs remains quite similar even varying the impact speed and impactor size, becoming steeper and more continuous (smaller size ratio between the two largest remnants) than the monolithic ones. This implies that at some point, more energy does not translate into a significantly different fragment SFD.

The largest remnant in rubble-pile simulations is (in general) smaller than that obtained for impacts into monolithic targets. This leads to a more continuous and steeper slope in the rubble-pile SFDs. A gradual change in the SFDs is observed (for impact angles up to 45°) with increasing impactor size, until $\log(M_{targ}/M_{imp}) > 1.8$ (impactors around 25 km).

Due to the similarities in the SFD for catastrophic disruption events, the SFD morphology alone is not particularly diagnostic of the circumstances of the impact event. The SFDs from sub-catastrophic events in contrast, produced by small impactors at impact angles smaller or equal to 45°, are sensitive to impact conditions (including parent body structure), and can potentially give us more information about the internal structure of a parent body than catastrophic or super-catastrophic events produced by large impactors.

4. Comparing simulation outcomes with observational data

In this section, we investigate whether the features seen in the modeled SFDs and satellite systems described in Section 3 share

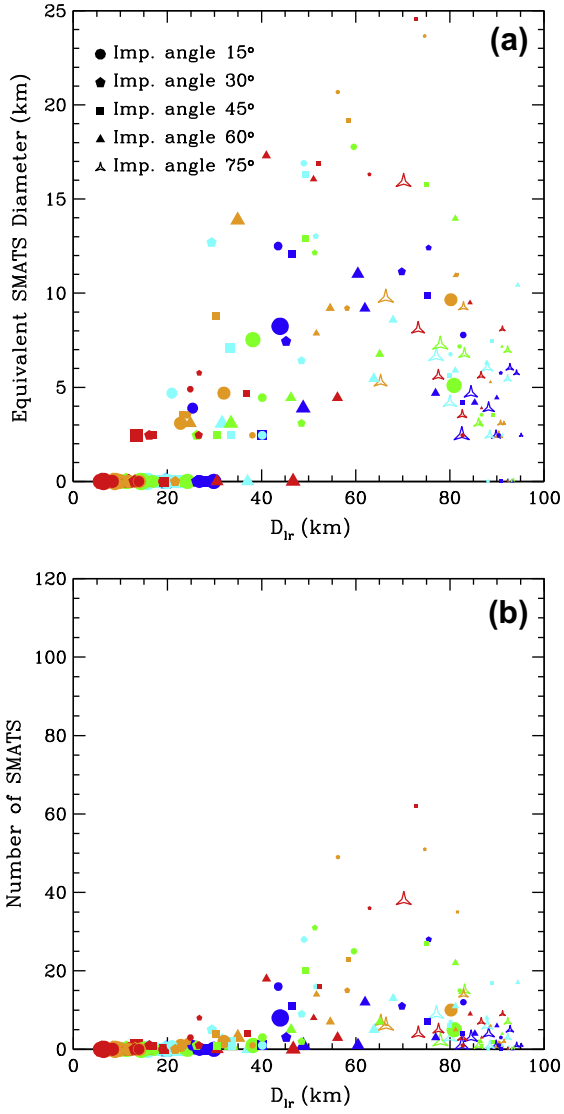

Fig. 4. (a) Equivalent SMATS diameter versus diameter of the largest remnant for rubble-pile targets. (b) Number of SMATS versus diameter of the largest remnant for rubble-pile targets. Color code indicates impact speed: blue corresponds to 3 km s^{-1}, cyan to 4 km s^{-1}, green to 5 km s^{-1}, orange to 6 km s^{-1} and red to 7 km s^{-1}. Symbol code indicates impact angles as is shown in the figure. Symbol sizes are coded according to impactor diameter, smaller dots represent smaller impactors (which size are: 7, 10, 14, 18, 25, 34 and 46 km).

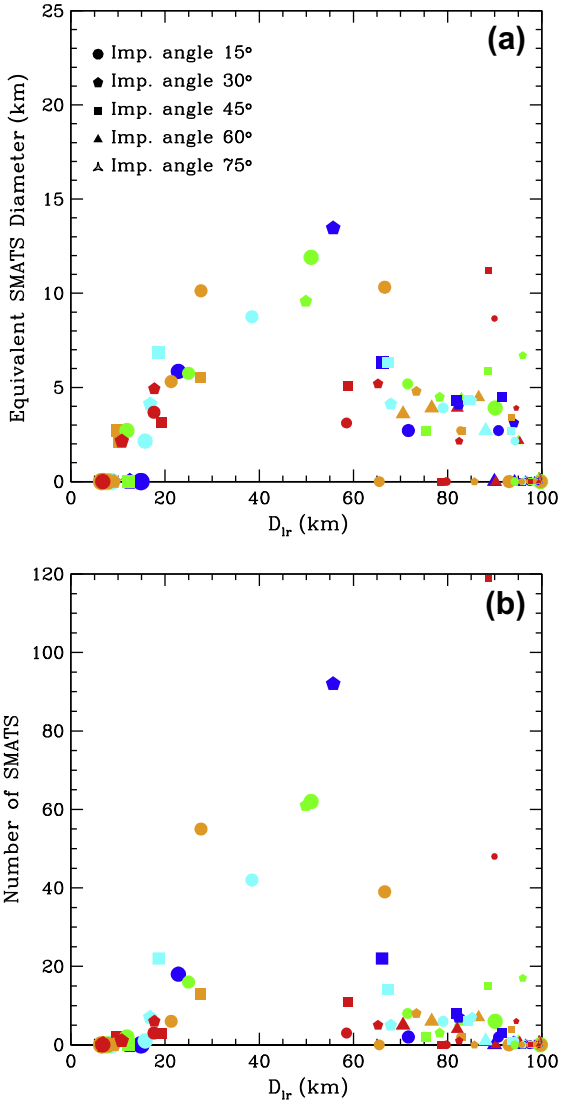

Fig. 5. (a) Equivalent SMATS diameter versus diameter of the largest remnant for monolithic targets. (b) Number of SMATS versus diameter of the largest remnant. Dot code is the same as in Fig. 4. Data for this figure are from simulations of Durda et al. (2004).

the same properties with observed main-belt family SFDs and binary asteroids.

4.1. Monolithic versus rubble-pile parent body

Significant debate and examples can be found in the literature about matching the size distribution of asteroid families with modeled SFDs by means of computer simulations. Most of the studied cases consider different internal structures (solid, shattered or porous targets) but for limited impact conditions, restricted to reproduce the SFD of a specific family. For example, the Karin family was investigated by Michel et al. (2004a) and then revisited by Nesvorný et al. (2006). Also, the Eunomia and Koronis families were studied by Michel et al. (2001, 2002, 2004a,b). Durda et al. (2007) systematically studied a complete grid of such parameters for monolithic targets (bulk density $\rho = 2.7$ g cm^{-3}) and compared the simulation results with actual asteroid families (Nesvorný et al., 2005). Here we extend this systematic study of fragment SFDs to rubble-pile parent bodies and also review the fit with solid targets (Durda et al., 2007) to decide in which cases rubble-pile SFDs achieve a better match.

Following Durda et al. (2007), the strategy applied to compare the SFDs can also be used to estimate the parent-body diameter of observed asteroid families by plotting the (morphologically matching) modeled SFD and the observed family SFD to the same scale on the same plot. This strategy assumes, of course, that impact outcomes are scalable to the observed families.[2]

As modeled impacts assumed a 100-km-diameter parent body, the resulting largest remnant and SFD of associated smaller

[2] This approximation appears to be reasonable (to zeroth order) for most observed families. However, it may well break down when the gravitational acceleration of the family's parent body is significantly larger or smaller than our modeled parent body. We are currently conducting new simulations with targets of 400 km and our preliminary results show some differences in the SFD respect to the same impact conditions with targets of 100 km.

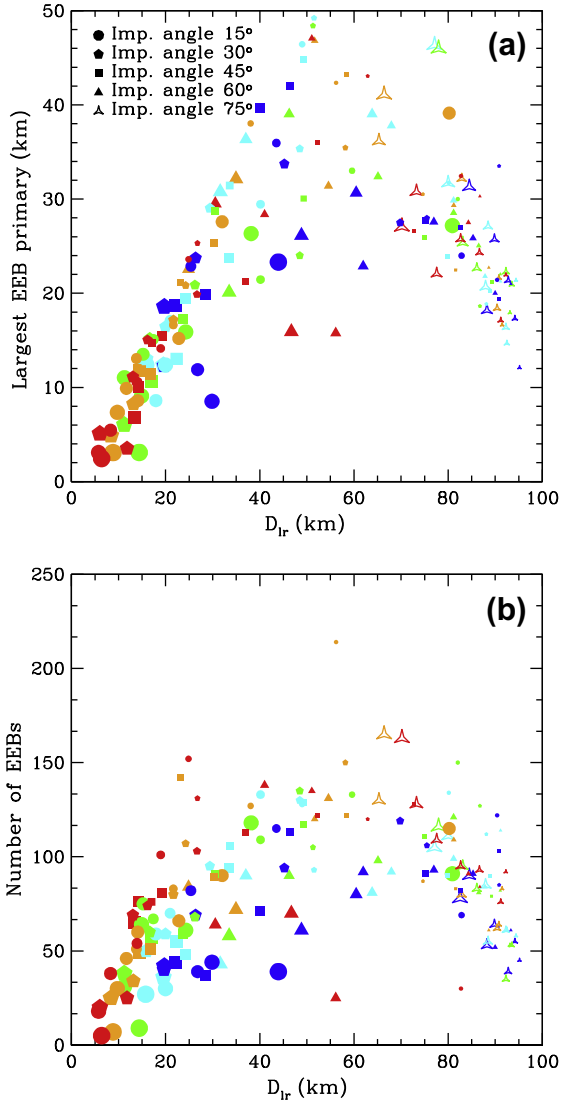

Fig. 6. (a) Largest EEB primary diameter versus diameter of largest remnant for rubble-pile case. (b) Number of EEB primaries versus diameter of largest remnant for rubble-pile case. Dot code is the same as in Fig. 4.

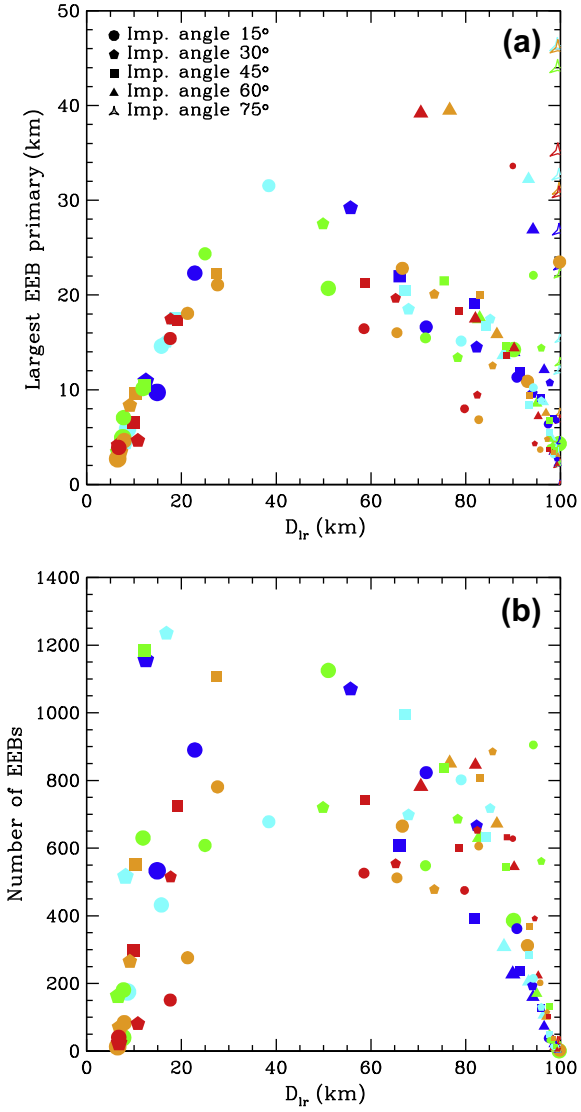

Fig. 7. (a) Largest EEB primary diameter versus diameter of largest remnant for monolithic case. (b) Number of EEB primaries versus diameter of largest remnant for monolithic case. Dot size code is the same as in Fig. 4. Data for this figure are from simulations of Durda et al. (2004).

fragments may need to be offset to the left or right to match the observed SFD, suggesting a larger or smaller parent body for the observed family, respectively. The magnitude of this offset in logarithmic units yields the factor to increase or decrease the diameter of the actual family parent body from the 100-km-diameter parent body of the modeled family. Hence, this method of deriving the actual family parent body diameter by scaling from our 100-km parent body simulation results assumes that the impact outcomes scale linearly with parent-body size.

We considered the same families studied by Durda et al. (2007) (see their Table 1), who applied the procedure detailed in Nesvorný et al. (2005) to determine families. Some of the families analyzed are suspected to have interlopers among the larger members, which can affect the shape of the observed family SFDs. When possible, such interlopers have been removed from the SFD before comparison with the modeled SFDs (see Table 1 in Durda et al. for more details about interlopers). For this task Durda et al. relied primarily on Cellino et al. (2002) for the list of family interlopers. In some cases they made some additional suggestions of interlopers based on perceived anomalies in the shapes of the size–frequency distributions, which could be somewhat subjective. Note that we did not include the Karin family in the analysis because Nesvorný et al. (2006) performed a more detailed study using similar codes and a revised Karin cluster membership to show that the disruption of an unfractured (monolithic) parent body produces the most satisfactory match to the observed Karin cluster SFD. We did not include the Nysa–Polana family because this structure corresponds to two impacts that are difficult to separate (Cellino et al., 2001).

We can group the results of our comparison in four classes. We identify families best explained by impacts with rubble-pile SFDs, the ones that fit better with monolithic SFDs, those that give a good fit to both cases, and finally those that are not well represented by either. In the following we discuss each one of these classes.

4.1.1. Rubble-pile parent body

The asteroid families that best fit with a rubble-pile parent body are Meliboea, Erigone, Misa, Agnia, Gefion and Rafita.

A graphical comparison of these cases is shown in Fig. 9. In Table 2 are listed the shift factor to match the actual family SFD

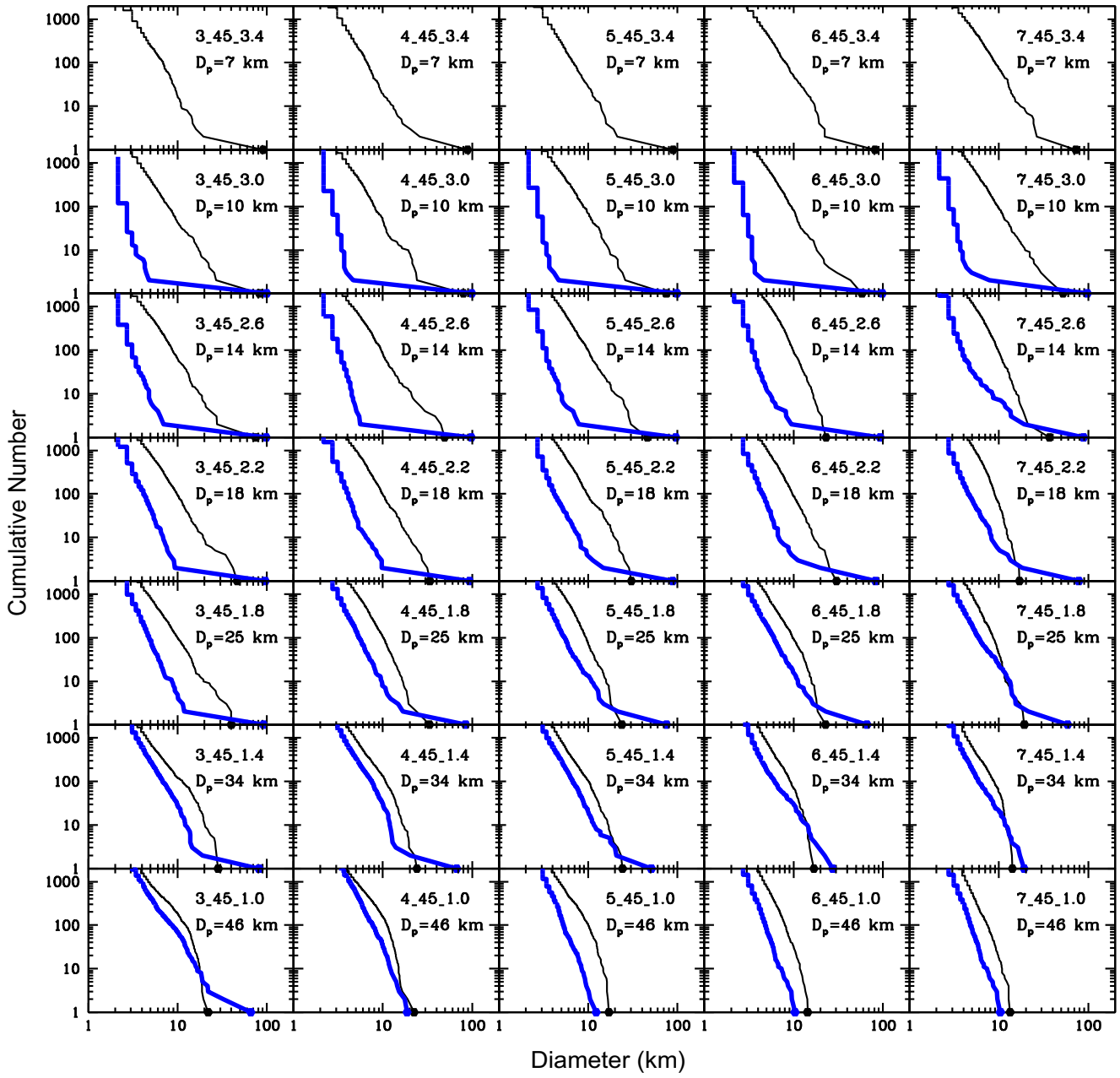

Fig. 8. Modeled rubble-pile (thin line) and monolithic (thick line) SFD for impact angle 45° (other impact angles simulated are shown in Appendix A).

and the re-calculated parent-body diameter. In general, the parent-body diameter is smaller than the one previously estimated from monolithic targets. All of theses families (except Gefion) are produced by cratering impacts. According to the results of the comparison of SFDs discussed in Section 3.3, the impact conditions for these families are in the parameter space that allows us to infer physical properties of the parent body. In contrast, Gefion is a family produced by a catastrophic disruption event. For this kind of high-energy impact, the monolithic and rubble-pile SFDs are usually close, but in this case a visual inspection of Fig. 9e shows that a rubble-pile parent body leads to a better fit than the monolithic one. Note that Durda et al. (2007) showed that they could not find a good fit for this family with monolithic parent bodies.

4.1.2. Monolithic parent body

For the following families, Hygiea, Massalia, Hestia, Nemesis, Sylvia and Eos, we could not obtain a better fit with rubble-pile simulations. Accordingly, we confirm the monolithic fit from Durda et al. (2007) regarding the impact conditions and physical properties of the parent body that could produce these families.

4.1.3. Similar fit

The following families, Eunomia, Themis, Adeona, Maria, Emma, Padua, Veritas, Koronis, Dora, Merxia, Naema, Bower, Hoffmeister and Lixiaohua are well matched by both monolithic and rubble-pile SFDs. The difficulty in inferring uniquely the characteristics of the parent body in some of these cases may be due to the original SFD having been substantially different than is observed now (e.g., families close to a mean motion resonances, such as the 3:1 for the Maria family for instance, allowing the loss of some fragments over time). Here it is possible to distinguish two subclasses according to the kind of events:

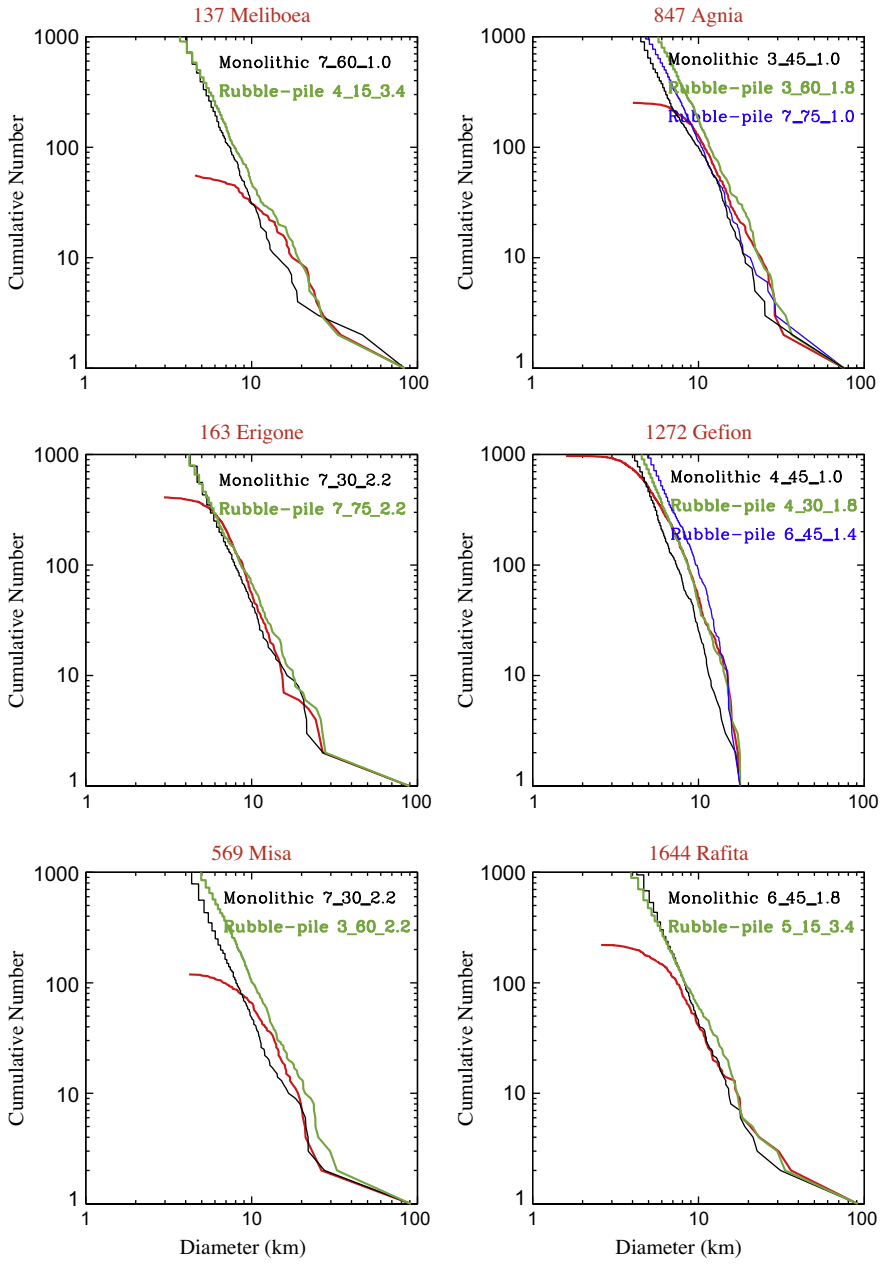

Fig. 9. Comparing the best monolithic and rubble-pile fit with observed families. Labels indicate the impact conditions that best fit the family SFD.

Table 2
Comparison of observed and modeled main-belt asteroid families.

Rubble-piles				
Family	Simulation	Shift factor	Mean parent diameter (km)	Spectral characteristics
137 Meliboea	4_15_3.4	1.81	181	C type
163 Erigone	7_75_2.2	0.88	88	C/X type
569 Misa	3_60_2.2	0.95	95	C type
847 Agnia	3_60_1.8	0.40	40	S type
1272 Gefion	4_30_1.8	1.75	175	S type
1644 Rafita	5_15_3.4	0.51	51	S type

- Cratering events (Maria, Padua, Naema, Adeona and Veritas): for these families, lower-energy or oblique impacts onto a rubble-pile targets are needed to reproduce the observed SFDs, in contrast to the high-energy impacts required for monolithic parent bodies.
- Catastrophic events (Koronis, Dora, Merxia, Bower, Hoffmeister and Lixiaohua): these families have a steep slope produced by high-energy impacts. For these families the SFD is very similar to both kinds of parent bodies studied, making it difficult to distinguish between them.

4.1.4. Any good fit

Finally there are four families that do not fit well enough with any modeled SFD. They are: Vesta, Flora, Brasilia and Chloris. Reasons for our inability to obtain a good fit could include the presence of interlopers (as was suggested by Durda et al. (2007) for the Brasilia and Chloris families), our solid and rubble-pile approximations did not adequately model the internal structure of the parent body, or the scaling to a 100-km target body was not appropriate. In the case of the Flora family, it lies on a dynamical diffusive background at the border of the asteroid belt and the family may have been significantly modified since formation. Also, the fact that it is difficult or impossible to find a very good fit for the Flora family can be related to the fact that Flora is very messy, and some members of the family could be really not reliable. On the other hand, Vesta is interesting because it is qualitatively special: a big crater on a very big object, and also due to its differentiated nature (Jutzi and Asphaug, 2011). This property of Vesta demands other kind of simulations.

We found that some asteroid families could have a rubble-pile progenitor and in general the impact conditions that best fit these families imply high impact speeds and oblique impact angles (both are indicated in the simulation name at the Fig. 9). The results presented here could support some previous works related to the alleged existence of bodies with a rubble-pile structure in the asteroid belt (Chapman, 1978; Farinella et al., 1981; Farinella et al., 1982). The most accepted explanation for how a primitive monolithic body becomes a rubble-pile is that a monolithic body suffered low-energy impacts during the early times of the asteroid belt, which could leave, a rubble-pile largest remnant almost as big as the original target, as indicate the results of Durda et al. (2004). Latter, when the asteroid belt was dynamically excited this kind of rubble-pile targets could be impacted again, but this time they suffer high-energy impacts. In this way the six families suggested to have a rubble-pile patent body could represent a second or third generation of the asteroid evolution.

The fraction of rubble-pile asteroids found among the largest main-belt asteroids ($D > 100$ km) is unknown for several reasons. First, we do not know the size of the projectile necessary to turn a large monolithic object into something that would be characterized as fractured, shattered, or shattered with rotated fragments (Richardson et al., 2002). It is possible that cratering events are enough to create rubble-piles rather than a catastrophic disruption event. If so, does the object remain a rubble-pile for the rest of its existence? Or do billions of years of smaller impacts and thermal recrystallizations gradually weld the object back together in some fashion so it no longer acts like a rubble-pile?

Second, the primordial history of the main asteroid belt from a collisional and dynamical standpoint is poorly understood. For example, some argue the asteroid belt started out fairly massive, with a large population of small objects needed to allow planetesimal formation to function between 2 and 3.2 AU (e.g. Cuzzi et al., 2010). This population was then mostly eliminated by dynamical processes within the first few Myr of the formation of the first solids (e.g., depletion of the gas disk causing resonances to sweep the region; the escape of planetary embryos formed in the main-belt zone; the potential migration of Jupiter across the main-belt zone (see Petit et al., 2002; Walsh et al., 2011). Note that some aspects of the degree of collision evolution produced by a massive early main-belt population was explored by Bottke et al. (2005), but not in terms of whether such collisions produce rubble-pile asteroids. They found the degree of main-belt collisional evolution was controlled by the mass and life span of the population ejected from the asteroid belt.With this said, depending on how planetary formation works, it is also conceivable that the asteroid belt was dynamically cold for the first few hundreds of Myr of its existence, with a planetesimal mass that was only slightly larger than its current population (e.g. Minton and Malhotra, 2010). If so, collisional evolution among main-belt asteroids hitting one another would have been minimal, and the production of rubble-piles via collisions would have been limited.

Finally, there is the possibility of external populations affecting the asteroid belt. For example, Gomes et al. (2005) suggest that a reconfiguration of the giant planets ~4 Gyr ago destabilized a population of comet-like planetesimals residing beyond the original orbit of Neptune. If true, and depending on the size distribution of the comets themselves, these scattered bodies may have hit numerous main-belt bodies and potentially could have produced many rubble-piles. Similarly, a fraction of this population should become embedded in the asteroid belt itself raising the possibility of even more collisional evolution (Levison et al., 2009). An even earlier possibility is that the main-belt region was hit by

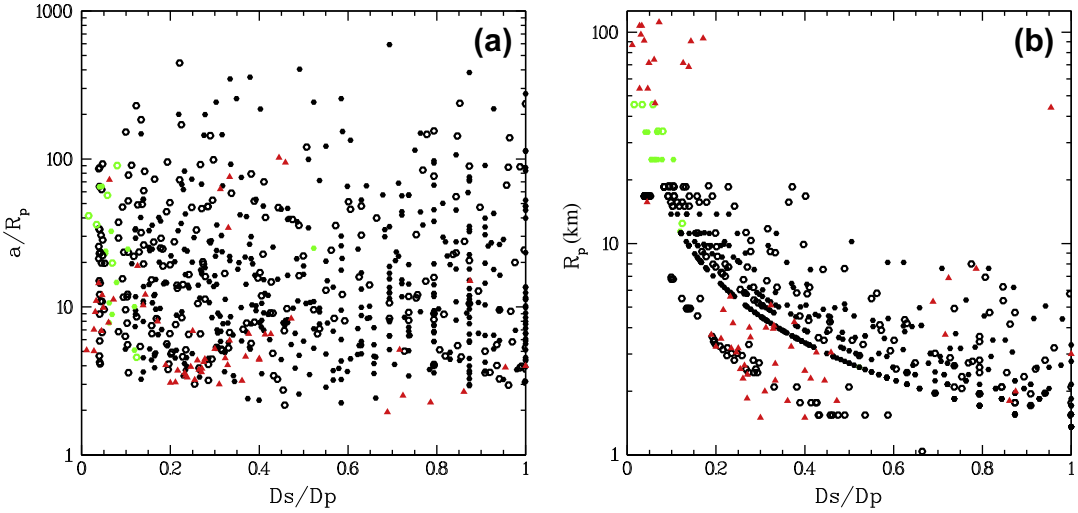

Fig. 10. (a) Relative component separation and (b) target radius versus secondary to primary diameter ratio for presently know main-belt binary asteroids (red triangles) (Johnston et al., 2010), SMATS (green dots) and EEBs (black dots) formed in the simulations. Open circles correspond to rubble-pile runs and fill circles correspond to monolithic runs. Monolithic and rubble-pile runs that best fits the Koronis, Themis, Emma and Flora families are included.

planetesimals scattered onto crossing orbits via growing planetary embryos within the terrestrial planet zone (e.g. Bottke et al., 2006) or by outer Solar System material scattered inward by a migrating Jupiter (Walsh et al., 2011). The degree of collisional evolution produced by these populations on the main-belt has yet to be examined.

4.2. Binary formation in the main-belt

The most common explanation of how large main-belt asteroids acquire satellites involves impacts followed by re-accumulation and capture (see Merline et al., 2002; Richardson and Walsh, 2006 for reviews of binary formation mechanisms). Among studied families, Themis, Koronis, Emma and Flora are known to have binary systems. In the case of the Themis family, two binaries have been found: (90) Antiope (Merline et al., 2000) and (379) Huenna (Margot, 2003). The Koronis family has three binary systems: (243) Ida-Dactyl, 17246 (2000 GL74) (Tamblyn et al., 2004) and 22899 (1999 TO14) (Merline et al., 2004), while only one system has been found in the Flora and Emma families; (3749) Balam and (283) Emma, respectively.

Fig. 10 shows the relative component separation (a/R_p, where a is the semi-major axis of the system and $R_p = D_p/2$) and R_p versus secondary-to-primary diameter ratio (D_s/D_p, where D_s and D_p indicate the secondary and primary component diameter) for SMATS and EEBs produced in rubble-pile and monolithic simulations that best fit the families observed to have at least a binary system. It is proper to mention that the trend shown by these runs are representative of all our matrix of simulations. Most SMATS are characterized by $D_s/D_p \leqslant 0.15$. While EEBs show a uniform distribution. Nearly all satellites have a/R_p above 2, but values up to 100 are relative rare.

All known main-belt binaries (Johnston et al., 2010) are also plotted on this figure. Nearly 78% of binaries have a/R_p less than

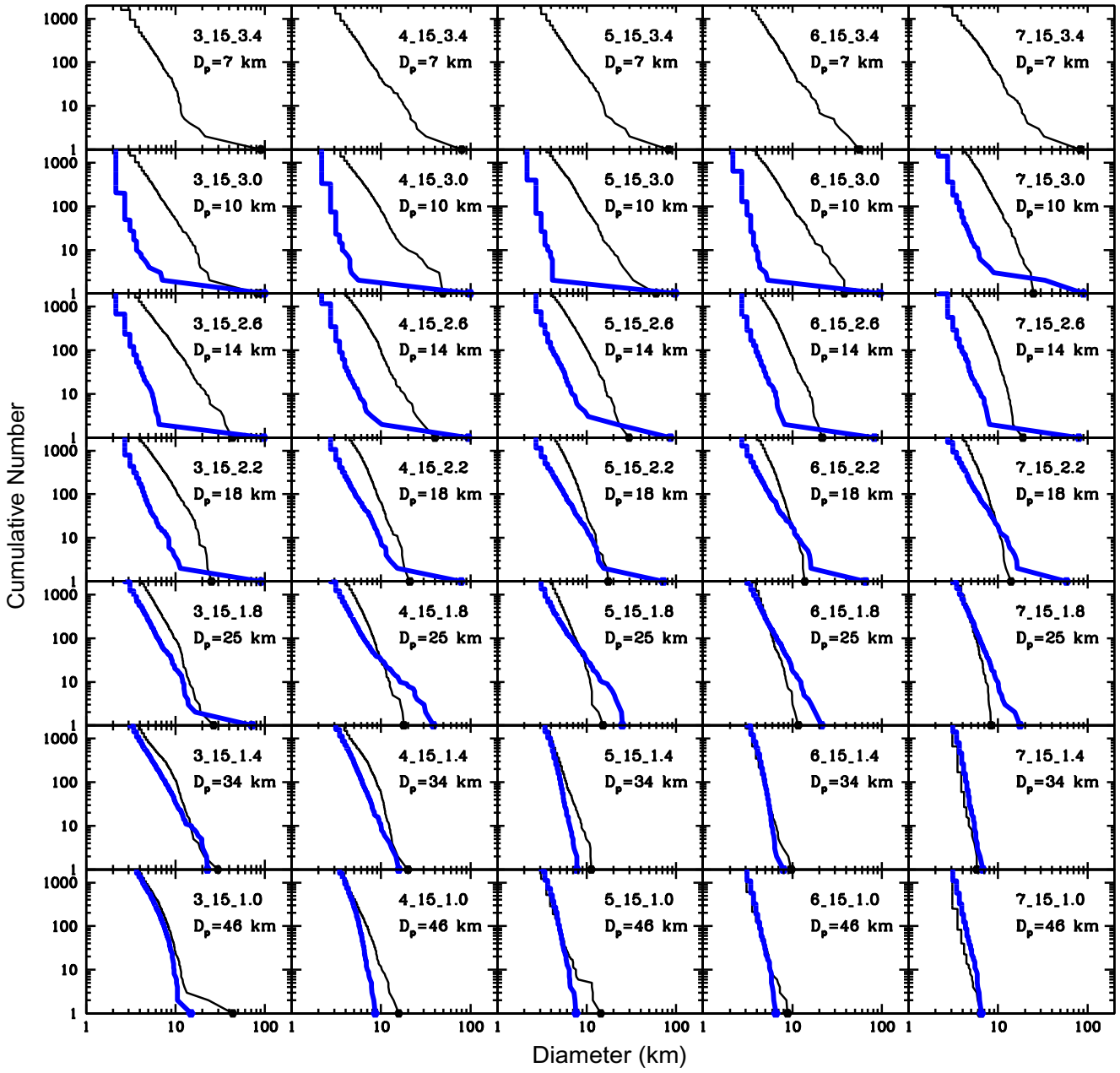

Fig. A.11. Modeled rubble-pile (thin line) and monolithic (thick line) SFDs.

10. In Fig. 10b three main subset of observed binary system are evident: those with $D_s/D_p < 0.2$; a big set between $0.2 < D_s/D_p < 0.5$; and some with $D_s/D_p > 0.6$. It is interesting to note that the second group match with a locus of rubble-pile EEBs. Nevertheless, Polishook et al. (2011) looked at the spin periods of the primaries of six observed systems that were good EEB candidates based on their small sizes and large separations. For five of the analyzed systems they find that the primaries are rapidly-spinning, making these systems good candidates for formation by YORP fission. While only one of the system that they studied is too big to be spun-up efficiently by the YORP effect and it rotate quite slowly to come from rotational-fission. We think the problem of identifying a single region in the Fig. 10, which could be related to a unique binary formation mechanism, could be due to two parameters: relative separation and size ratio alone are no sufficient to fully distinguish between various formation models.

There is a group of observed binaries with $D_s/D_p < 0.2$ and large primary body that does not match with simulated SMATS or EEBs, but follows the trend clearly. We suspect that these are the results of large cratering impacts and still are smaller than the impacts we have simulated in this work.

Simulations produce many satellites with larger relative separation than observed in the current main-belt binary population. Walsh and Richardson (2006) also noted this effect in the near-Earth asteroid population. They suggested a strong observational selection effect or evolutionary/survival considerations. We also observe a lack of detected binaries in the region $D_s/D_p > 0.5$ and $a/R_p > 10$. More than half of the binary asteroids found to date have been discovered using adaptive optics, which is more sensitive to detecting distant companions with a wide range of size-ratios. Our simulations suggest that many such binaries remain undetected or that some post-formation evolutionary mechanism is acting to bring components closer after binary formation.

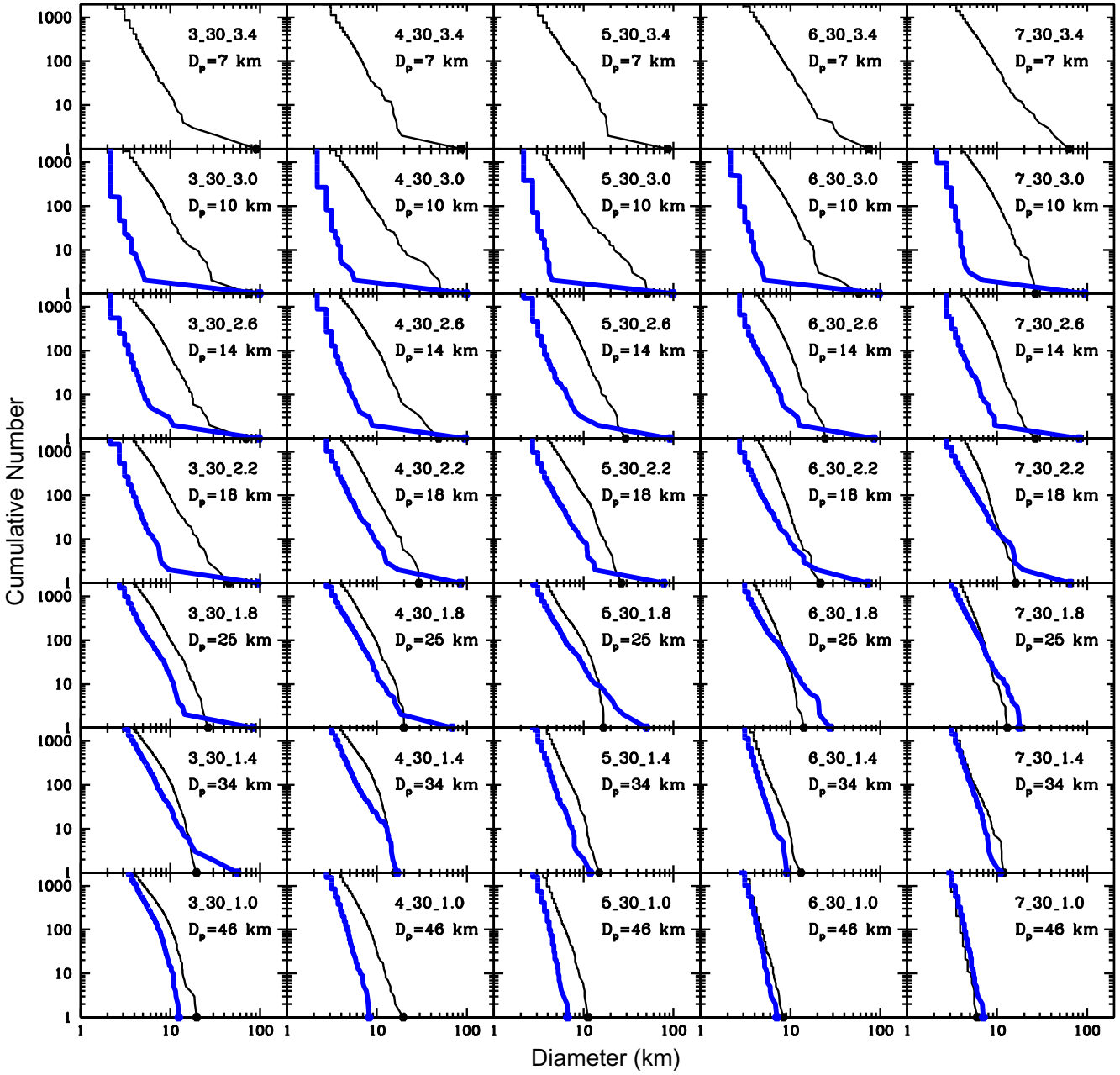

Fig. A.11. (*continued*)

5. Conclusions

In this paper we have analyzed, in a systematic way, the mean features resulting from impacts on both rubble-pile and monolithic parent bodies of 100 km in size. We have used the results to attempt to constrain the impact conditions at the origin of known asteroid families and observed binary systems according to the internal structure of their parent bodies. From our analysis we can draw the following conclusions.

Cratering events, produced by small impactors at angles $\leqslant 45°$, can give more information about the internal structure of the parent body than catastrophic or super-catastrophic events produced by large impactors. Comparing the SFDs from simulations of impacts into monolithic and rubble-pile target bodies with those from observed main-belt asteroid families, we identified six main-belt families (Meliboea, Erigone, Misa, Agnia, Gefion and Rafita) that are best represented by rubble-pile SFDs. For all these families the estimated parent body is smaller than the values estimated by Durda et al. (2007) for monolithic targets. On average, the slopes of simulated SFDs seem somewhat steeper than the actual family SFDs; given that they could suffer some collisional evolution or Yarkovsky-driven removal, this suggests that the primordial SFDs of families should be steeper than the currently observed ones. We did not observe any correlation between the taxonomic classification for each family and the properties of the parent body. In fact, of the six families that were found to likely come from a rubble-pile body, three of them are S-type (Agnia, Gefion and Rafita), while Meliboea is Ch-type, Erigone is C/X-type and Misa is C-type. In the same way, families identified as coming most plausibly from a monolithic parent body also belong to C and S taxonomic class.

We find that rubble-pile targets are less efficient at producing SMATS and EEBs than their monolithic target counterparts. Therefore, it is not surprising that binaries have not yet been found in

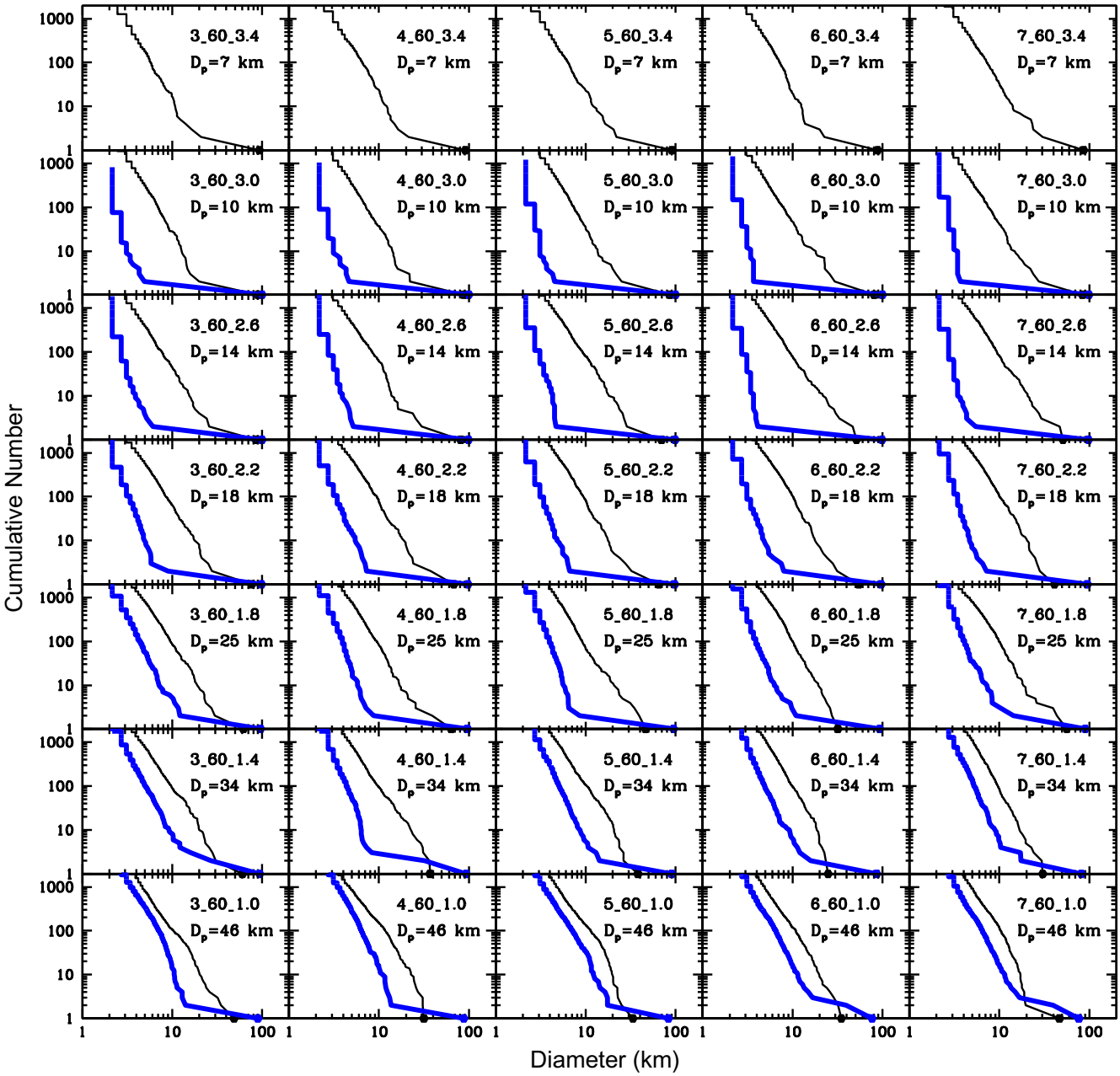

Fig. A.11. (*continued*)

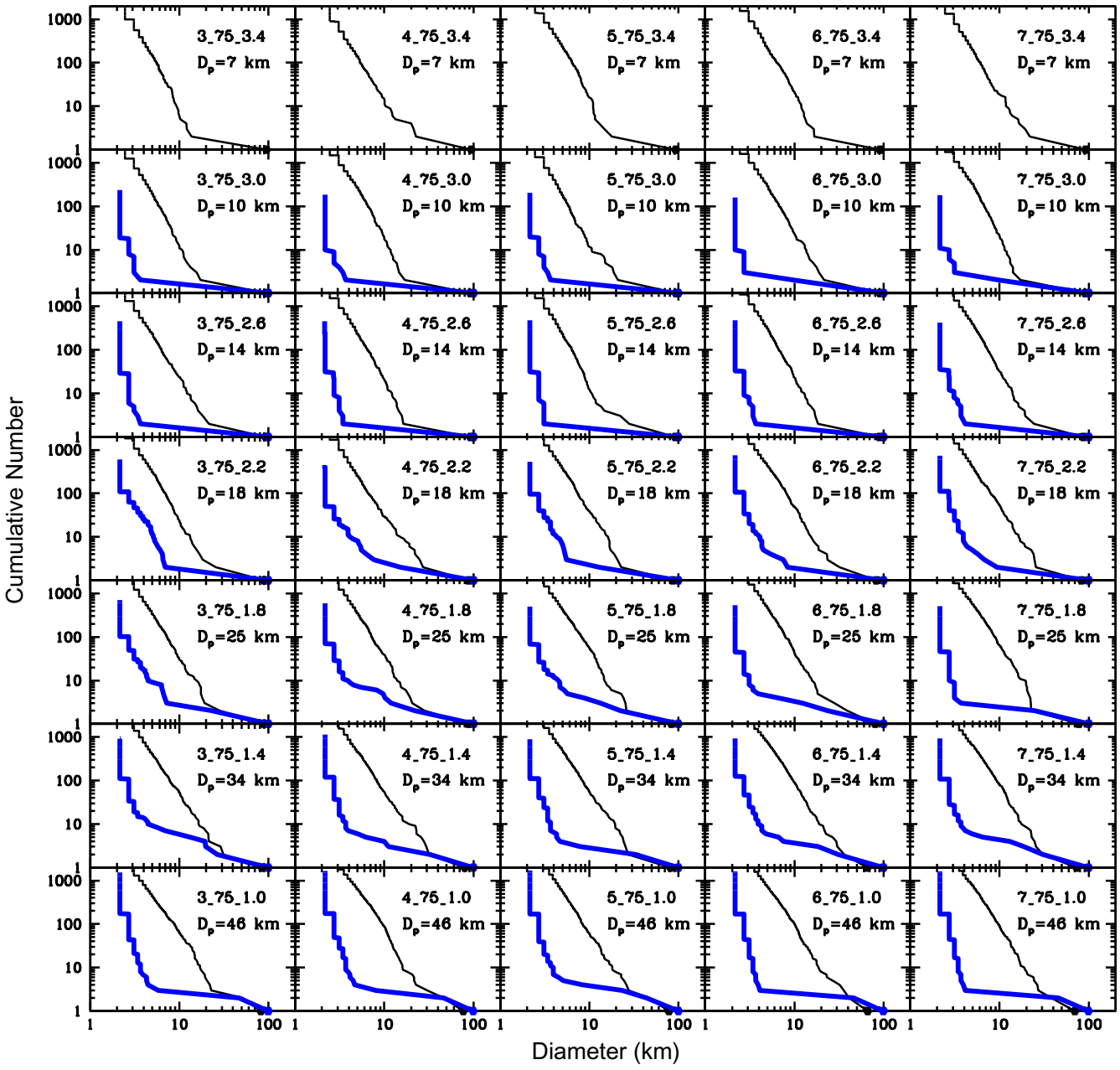

Fig. A.11. (*continued*)

families identified as originating from a rubble-pile parent body. We note, however, that satellites formed from both kinds of targets share similar characteristics. We also note that many main-belt binary systems closely resemble our simulated systems in size and orbital properties, suggesting that they could be formed during impact events, but these parameters alone are not conclusive. Many close binaries with small primaries are likely produced without collisions, such as by YORP (Bottke et al., 2002). The shapes and rotations rates of the primaries in observed EEB candidate systems indicate that some of these systems may well have been formed by the rotational spin-up and fission process due to YORP (Polishook et al., 2011), even though they over plot the collisional EEBs from our models. Although we have not tracked the resulting rotation rates of the components in collisional EEBs in our models to date, this is clearly a parameter that may help to distinguish between these collisional and rotational fission formation mechanisms. Finally, we are still unable to reproduce extreme binary systems, such as (90) Antiope. These kinds of systems might be produced by other means or may require more refined impact models incorporating more sophisticated equations of state for porous materials and/or impact parameters that we have not modeled here.

Our model also produces satellites around the other large remnants (second-largest, third-largest, etc.) that are themselves reaccumulated bodies, also leading us to conclude that the formation of SMATS and EEBs may be considered more continuous in this region.

From a broader perspective, the answer to whether the asteroid belt is dominated by monolithic/shock-annealed objects, fragmented objects, or rubble-piles continues to elude us, mainly because there is no obvious test to tell one from the other beyond crude measures like bulk density, etc. For example, consider (4) Vesta, a 530 km diameter asteroid that has now been extensively imaged by the DAWN spacecraft (Jaumann, submitted for publication). Vestas shape is defined by a huge, 500 km diameter basin

located Near Vesta's south pole. The blast that made this basin also probably produced a series of troughs near Vestas equator. Given this evidence, one might think it is obvious that Vesta is a rubble-pile. Perhaps, but how does one prove it in a quantitative manner?

Consider that the bulk density of Vesta (i.e., 3.42 g cm^{-3}; Baer and Chesley, 2008) is not unusually low compared to those meteorites believed to come from Vesta (e.g., the eucrites have bulk densities near 3 g cm^{-3}; Britt et al., 2010). This implies this impact event, as large as it was, did not produce an abundance of macroporosity in the target body. The equatorial troughs almost certainly imply that Vesta once had a fractured interior, yet subsequent shocks from impacts might have welded these putative internal fractures back together again. If so, the fossils of a fractured interior may not tell us much about current conditions. The surface damage and ejecta produced by this major basin-forming event, when fully measured, is likely to be considerable, yet these components cannot yet be used to infer Vestas internal structure (though they might when more modeling work is completed). Thus, unless some other diagnostic feature of fractured or rubble-pile asteroids comes to the fore, or we find a way to place seismometers on Vestas surface, it is hard to use what we know about Vesta to infer its present-day internal structure. Similarly, despite the fact that the asteroid belt has likely experienced considerable collisional evolution, and this paper's finding that rubble-piles disrupt more easily than monolithic targets, we have yet to find a "smoking gun" telling us that most large bodies behave like rubble-piles in large-scale collision events. Our search will go on as we take advantage of our improved knowledge of both asteroid families and how they collisionally/dynamically evolved over main belt history.

5.1. Future work

We are aware that the "shift" technique applied to estimate the size of the parent body could be not accurate enough because the gravitational effect changes for different sizes. Therefore we plan to perform new runs designated to study smaller and larger parent bodies ($D \ll 100$ km and $D \gg 100$ km). We also found in this work that (90) Antiope system is very hard to reproduce with the current simulations. We think that simulating the impact of target with size closer to the suspected size of the Themis parent body, including a new N-body model with bouncing/merging parameter, could allow us to draw more reliable conclusions about the formation mechanism for this intriguing binary system.

Acknowledgments

This project is supported by National Science Foundation Grant AST0708517. This work was done while the first author was spending a stay at SwRI. P.G.B. acknowledges the Generalitat Valenciana (Consellería de Educación) for providing the financial support for this long-term visit and the partially suport by Spanish grant AYA2008-06202-C03-03. D.C.R. acknowledges support by the National Aeronautics and Space Administration under Grant No. NNX08AM39G issued through the Office of Space Science. E.A. thanks the NASA Planetery Geology and Geophysics Program. W.J.M. acknowledges the NASA and NSF Planetary Astronomy Programs. We appreciate the comments from A. Cellino and an anonymous reviewer that helped to improve this manuscript.

Appendix A. SFD for others impacts angles

Here the Fig. 8 is shown for impact angles of 15°, 30°, 60° and 75° (see Fig. A.11).

References

Asphaug, E., Melosh, H.J., 1993. The Stickney impact of Phobos: A dynamical model. Icarus 101, 144–164.
Asphaug, E., Ryan, E.V., Zuber, M.T., 2002. Asteroid interiors. In: Bottke, W.F., Cellino, A., Paolicchi, P., Binzel, R.P. (Eds.), Asteroids III. Univ. of Arizona Press, Tucson, pp. 463–484.
Baer, J., Chesley, S.R., 2008. Astrometric masses of 21 asteroids, and an integrated asteroid ephemeris. Celest. Mech. Dynam. Astron. 100, 27–42.
Barnes, J., Hut, P., 1986. A hierarchical O(N log$N$) force-calculation algorithm. Nature 324, 446–449.
Benz, W., Asphaug, E., 1994. Impact simulations with fracture: I. Method and tests. Icarus 107, 98–116.
Benz, W., Asphaug, E., 1995. Simulations of brittle solids using smooth particle hydrodynamics. Comput. Phys. Commun. 87, 253–265.
Bottke Jr., W.F., Vokrouhlický, D., Rubincam, D.P., Broz, M., 2002. The effect of Yarkovsky thermal forces on the dynamical evolution of asteroids and meteoroids. In: Bottke, W.F., Cellino, A., Paolicchi, P., Binzel, R.P. (Eds.), Asteroids III. Univ. of Arizona Press, Tucson, pp. 395–408.
Bottke, W.F., Durda, D.D., Nesvorný, D., Jedicke, R., Morbidelli, A., Vokrouhlický, D., Levison, H., 2005. The fossilized size distribution of the main asteroid belt. Icarus 175, 111–140.
Bottke, W.F., Nesvorný, D., Grimm, R.E., Morbidelli, A., O'Brien, D.P., 2006. Iron meteorites as remnants of planetesimals formed in the terrestrial planet region. Nature 439, 821–824.
Britt, D.T., Consolmagno, G.J., 2000. The porosity of dark meteorites and the structure of low-albedo asteroids. Icarus 146, 213–219.
Britt, D., Macke, R., Consolmagno, G., 2010. The Density, Porosity, and Structure of Very Small Bodies. European Planetary Science Congress 2010, pp. 863–863.
Campo Bagatin, A., Petit, J.-M., 2001a. How many rubble piles are in the asteroid belt? Icarus 149, 198–209.
Campo Bagatin, A., Petit, J.-M., 2001b. Effects of the geometric constraints on the size distributions of debris in asteroidal fragmentation. Icarus 149, 210–221.
Chapman, C.R., 1978. Asteroid collisions, craters, regolith, and lifetimes. In: NASA Conference Publication, 2053, pp. 145–160.
Cellino, A., Pannunzio, R., Zappala, V., Farinella, P., Paolicchi, P., 1985. Do we observe light curves of binary asteroids? Astron. Astrophys. 144, 355–362.
Cellino, A., Zappalà, V., Doressoundiram, A., di Martino, M., Bendjoya, P., Dotto, E., Migliorini, F., 2001. The puzzling case of the Nysa–Polana family. Icarus 152, 225–237.
Cellino, A., Bus, S.J., Doressoundiram, A., Lazzaro, D., 2002. Spectroscopic properties of asteroid families. In: Bottke, W.F., Cellino, A., Paolicchi, P., Binzel, R.P. (Eds.), Asteroids III. Univ. of Arizona Press, Tucson, pp. 633–643.
Cuzzi, J.N., Hogan, R.C., Bottke, W.F., 2010. Towards initial mass functions for asteroids and Kuiper belt objects. Icarus 208, 518–538.
Doressoundiram, A., Paolicchi, P., Verlicchi, A., Cellino, A., 1997. The formation of binary asteroids as outcomes of catastrophic collisions. Planet. Space Sci. 45, 757–770.
Durda, D.D., 1996. The formation of asteroidal satellites in catastrophic collisions. Icarus 120, 212–219.
Durda, D.D., Bottke, W.F., Enke, B.L., Merline, W.J., Asphaug, E., Richardson, D.C., Leinhardt, Z.M., 2004. The formation of asteroid satellites in large impacts: Results from numerical simulations. Icarus 170, 243–257.
Durda, D.D., Bottke, W.F., Nesvorný, D., Enke, B.L., Merline, W.J., Asphaug, E., Richardson, D.C., 2007. Size–frequency distributions of fragments from SPH/N-body simulations of asteroid impacts: Comparison with observed asteroid families. Icarus 186, 498–516.
Farinella, P., Paolicchi, P., Zappala, V., 1981. Analysis of the spin rate distribution of asteroids. Astron. Astrophys. 104, 159–165.
Farinella, P., Paolicchi, P., Zappala, V., 1982. The asteroids as outcomes of catastrophic collisions. Icarus 52, 409–433.
Fujiwara, A. et al., 2006. The rubble-pile asteroid Itokawa as observed by Hayabusa. Science 312, 1330–1334.
Gomes, R., Levison, H.F., Tsiganis, K., Morbidelli, A., 2005. Origin of the cataclysmic Late Heavy Bombardment period of the terrestrial planets. Nature 435, 466–469.
Hartmann, W.K., 1979. Diverse puzzling asteroids and a possible unified explanation. Asteroids. Univ. of Arizona Press, Tucson, pp. 466–479.
Jaumann, R. et al., Submitted for publication. Vestas Shape and Morphology. Science.
Johnston, W.R., Richardson, D.C., Walsh, K.J., 2010 Binary Minor Planets V3.0. EAR-A-COMPIL-5-BINMP-V3.0. NASA Planetary Data System.
Jutzi, M., Asphaug, E., 2011. Mega-ejecta on asteroid Vesta. Geophys. Res. Lett. 38, L01102.
Jutzi, M., Michel, P., Benz, W., Richardson, D.C., 2010. Fragment properties at the catastrophic disruption threshold: The effect of the parent body's internal structure. Icarus 207, 54–65.
Leinhardt, Z.M., Richardson, D.C., Quinn, T., 2000. Direct N-body simulations of rubble pile collisions. Icarus 146, 133–151.
Leinhardt, Z.M., Richardson, D.C., 2002. N-body simulations of planetesimal evolution: Effect of varying impactor mass ratio. Icarus 159, 306–313.
Leinhardt, Z.M., Richardson, D.C., 2005. A fast method for finding bound systems in numerical simulations: Results from the formation of asteroid binaries. Icarus 176, 432–439.
Leinhardt, Z.M., Stewart, S.T., 2009. Full numerical simulations of catastrophic small body collisions. Icarus 199, 542–559.

Leinhardt, Z.M., Marcus, R.A., Stewart, S.T., 2010. The formation of the collisional family around the dwarf planet Haumea. Astrophys. J. 714, 1789–1799.
Levison, H.F., Bottke, W.F., Gounelle, M., Morbidelli, A., Nesvorný, D., Tsiganis, K., 2009. Contamination of the asteroid belt by primordial trans-Neptunian objects. Nature 460, 364–366.
Margot, J.L., 2003. S/2003 (379) 1. IAU Circ., 8182, p. 1.
Melosh, H.J., 1989. Impact Cratering: A Geologic Process. Oxford University Press, New York.
Merline, W.J. et al., 2000. Discovery of companions to Asteroids 762 Pulcova and 90 Antiope by direct imaging. Bull. Am. Astron. Soc. 32, 1017.
Merline, W.J., Weidenschilling, S.J., Durda, D.D., Margot, J.L., Pravec, P., Storrs, A.D., 2002. Asteroids do have satellites. In: Bottke, W.F., Cellino, A., Paolicchi, P., Binzel, R.P. (Eds.), Asteroids III. Univ. of Arizona Press, Tucson, pp. 289–312.
Merline, W.J. et al., 2004. S/2004 (4674) 1. IAU Circ., 8297, p. 1.
Michel, P., Benz, W., Tanga, P., Richardson, D.C., 2001. Collisions and gravitational reaccumulation: Forming asteroid families and satellites. Science 294, 1696–1700.
Michel, P., Tanga, P., Benz, W., Richardson, D.C., 2002. Formation of asteroid families by catastrophic disruption: Simulations with fragmentation and gravitational reaccumulation. Icarus 160, 10–23.
Michel, P., Benz, W., Richardson, D.C., 2003. Disruption of fragmented parent bodies as the origin of asteroid families. Nature 421, 608–611.
Michel, P., Benz, W., Richardson, D.C., 2004a. Catastrophic disruption of pre-shattered parent bodies. Icarus 168, 420–432.
Michel, P., Benz, W., Richardson, D.C., 2004b. Catastrophic disruption of asteroids and family formation: A review of numerical simulations including both fragmentation and gravitational reaccumulations. Planet. Space Sci. 52, 1109–1117.
Minton, D.A., Malhotra, R., 2010. Dynamical erosion of the asteroid belt and implications for large impacts in the inner Solar System. Icarus 207, 744–757.
Nesvorný, D., Jedicke, R., Whiteley, R.J., Ivezić, Ž., 2005. Evidence for asteroid space weathering from the Sloan Digital Sky Survey. Icarus 173, 132–152.
Nesvorný, D., Enke, B.L., Bottke, W.F., Durda, D.D., Asphaug, E., Richardson, D.C., 2006. Karin cluster formation by asteroid impact. Icarus 183, 296–311.
Paolicchi, P., Cellino, A., Farinella, P., Zappala, V., 1989. A semiempirical model of catastrophic breakup processes. Icarus 77, 187–212.
Paolicchi, P., Verlicchi, A., Cellino, A., 1996. An improved semi-empirical model of catastrophic impact processes. I: Theory and laboratory experiments. Icarus 121, 126–157.
Petit, J.-M., Chambers, J., Franklin, F., Nagasawa, M., 2002. Primordial excitation and depletion of the main belt. In: Bottke, W.F., Cellino, A., Paolicchi, P., Binzel, R.P. (Eds.), Asteroids III. Univ. of Arizona Press, Tucson, pp. 711–723.
Polishook, D., Brosch, N., Prialnik, D., 2011. Rotation periods of binary asteroids with large separations – Confronting the Escaping Ejecta Binaries model with observations. Icarus 212, 167–174.
Richardson, D.C., Quinn, T., Stadel, J., Lake, G., 2000. Direct large-scale N-body simulations of planetesimal dynamics. Icarus 143, 45–59.
Richardson, D.C., Leinhardt, Z.M., Melosh, H.J., Bottke Jr., W.F., Asphaug, E., 2002. Gravitational aggregates: Evidence and evolution. In: Bottke, W.F., Cellino, A., Paolicchi, P., Binzel, R.P. (Eds.), Asteroids III. Univ. of Arizona Press, Tucson, pp. 501–515.
Richardson, D.C., Walsh, K.J., 2006. Binary minor planets. Ann. Rev. Earth Planet. Sci. 34, 47–81.
Richardson, D.C., Walsh, K.J., Murdoch, N., Michel, P., 2011. Numerical simulations of granular dynamics. I. Hard-sphere discrete element method and tests. Icarus 212, 427–437.
Stadel, J.G., 2001. Cosmological N-body simulations and their analysis. Thesis, University of Washington, Seattle.
Sullivan, R.J., Thomas, P.C., Murchie, S.L., Robinson, M.S., 2002. Asteroid geology from Galileo and NEAR Shoemaker data. In: Bottke, W.F., Cellino, A., Paolicchi, P., Binzel, R.P. (Eds.), Asteroids III. Univ. of Arizona Press, Tucson, pp. 331–350.
Tanga, P., Cellino, A., Michel, P., Zappalà, V., Paolicchi, P., dell'Oro, A., 1999. On the size distribution of asteroid families: The role of geometry. Icarus 141, 65–78.
Tanga, P. et al., 2009. Rubble-pile reshaping reproduces overall asteroid shapes. Astrophys. J. Lett. 706, 197–202.
Tamblyn, P.M. et al., 2004. S/2004 (17246) 1. IAU Circ., 8293, p. 3.
Tillotson, J.H., 1962. Metallic equations of state for hypervelocity impact. General Atomic Report GA-3216.
Walsh, K.J., Richardson, D.C., 2006. Binary near-Earth asteroid formation: Rubble pile model of tidal disruptions. Icarus 180, 201–216.
Walsh, K.J., Morbidelli, A., Raymond, S.N., O'Brien, D.P., Mandell, A.M., 2011. A low mass for Mars from Jupiter's early gas-driven migration. Nature 475, 206–209.